Spatial changes in gas transport and sediment stiffness influenced by regional stress: observations from piezometer data along Vestnesa Ridge, eastern Fram Strait

A. Plaza-Faverola[1], N. Sultan[2], R. G. Lucchi[1,3], N. El bani Altuna[1], H. Ramachandran[1], S. Singhroha[1], F. Cooke[1], S. Vadakkepuliyambatta[1,4], M. M. Ezat[1], and T. L. Rasmussen[1]

[1] CAGE-Centre for Arctic Gas Hydrate, Environment, and Climate, Department of Geosciences, UiT-the Arctic University of Norway, Tromsø, Norway

[2] Geo-Ocean, UMR6538, Ifremer, CNRS, UBO, UBS, 29280 Plouzané, France

[3]National Institute of Oceanography and Applied Geophysics – OGS, Trieste, Italy

[4] National Centre for Polar and Ocean Research, Ministry of Earth Sciences, Vasco-da-Gama, Goa, India.

Corresponding author: Andreia Plaza-Faverola (andreia.a.faverola@uit.no)

Key Points:

- This study documents in-situ pore pressure measurements along the gas charged Vestnesa sedimentary ridge in the eastern Fram Strait.
- Integrated piezometer and calypso core analyses indicate spatial variations in sediment stiffness and localized excess pore pressures.
- Gas transport and sub-seabed sediment stiffness are interrelated and affected by sea-level changes and fault behavior.

Abstract

Gas transport through sediments to the seabed and seepage occurs via advection through pores, faults, and fractures, and as solubility driven gas diffusion. The pore pressure gradient is a key factor in these processes. Yet, in-situ measurements for quantitative studies of fluid dynamics and sediment deformation in deep ocean environments remain scarce. In this study, we integrate piezometer data, geotechnical tests, and sediment core analyses to study the pressure regime that controls gas transport along the Vestnesa Ridge in the eastern Fram Strait. The data show a progressive westward decrease in induced pore pressure (i.e., from c. 180 to c. 50 kPa) upon piezometer penetration and undrained shear strength of the sediments, interpreted as a decrease in sediment stiffness. In addition, the data suggest that the upper c. 6 m of sediments may be mechanically damaged due to variations in gas diffusion rates and exsolution. Background pore pressures are mostly at hydrostatic conditions, but localized excess pore pressures (i.e., up to 10 kPa) exist and point towards external controls. When analyzed in conjunction with observations from geophysical data and sediment core analyses, the pore pressure data suggest a spatial change from an advection dominated to a diffusion dominated fluid flow system, influenced by the behavior of sedimentary faults. Understanding gas transport mechanisms and their effect on fine-grained sediments of deep ocean settings is critical for constraining gas hydrate inventories, seepage phenomena and sub-seabed sediment deformations and instabilities.

Plain Language Summary

Seafloor methane seepage occurs persistently in response to pressure changes. The scarcity of sub-seabed pressure data limits our understanding of the mechanisms of methane release. Here we document observations from 4 days monitoring of pressure and temperature within the upper 10 m of sediment at a seepage site in the Fram Strait. The survey extends for 60 km between the continental shelf off west-Svalbard and the mid-ocean ridge. The data show that the geothermal gradient increases and that sub-seabed sediments become softer and more susceptible to deformation as they approach the mid-ocean ridge. When analyzed in conjunction with cross-disciplinary data it seems plausible that the changes in sediment properties are associated with an increase in the amount of dissolved methane transported to the seafloor. We suggest that changes in the geological setting have resulted in the locking of fractures that would otherwise allow the release of trapped methane to the ocean. Trapped gas in the sediment pores is pumped by tides and causes damages beneath the seafloor. This study is an important step in understanding the mechanisms involved in the transport of methane into the ocean, with implications for climate research, assessment of geological hazards and alternative energy resources.

1 Introduction

Fine-grained marine sediments along continental slopes and rises are saturated with gas rich fluids. The mechanisms of gas transport from the source towards the seafloor influence the sediment geomechanical properties as well as gas hydrate accumulations and seepage dynamics [e.g., Clennell et al., 2000; Liu and Flemings 2006; Fleischer et al., 2001; Hong et al., 2019; VanderBeek and Rempel, 2018]. Free gas can be transported by advection through coarse grained layers (capillary invasion) or through permeable conduits like faults and fractures [Jain and Juanes, 2009; Terzariol et al., 2021]. Gas is transported primarily by diffusion, a process driven by changes in dissolved gas concentrations within the pore space [e.g., Gupta et al., 2021; VanderBeek and Rempel, 2018 and references therein]. Diffusive free-gas flow may affect the hydro-mechanical properties of the sediments without impacting the seabed morphology. Sediment strength and free-gas dynamics have a coupled relationship. While sediment properties control gas nucleation and migration [Boudreau et al., 2005; Johnson et al., 2002; Sills et al., 1991; Terzariol et al., 2021; Zhou and Katsman, 2022], gas exsolution/dissolution and expansion/compression [Sobkowicz and Morgenstern, 1984] may alter the properties of the host sediments (e.g., elastic and mechanical properties [Barry et al., 2010; Boudreau, 2012]), its compressibility [Blouin et al., 2019; Puzrin et al., 2011; Thomas, 1987] and its shear strength [Hight and Leroueil, 2003; Lunne et al. 2001; Sultan et al., 2012; Wheeler, 1988].

A critical factor driving gas migration towards the sub-seabed and into the ocean is the pore pressure gradient which highly affects the strength and mechanical response of the sediment to regional and local forcing [e.g., Bolton and Maltman, 1998]. The relation between pore pressures and in situ principal stresses generated by tectonic forcing determines the fluid flow regime through the sediments. Excess pore pressures (i.e., pressures above hydrostatic pressure) lead to shearing if the background tectonic stress regime is transpressive, or to tensile fracturing under an extensional stress regime [Bolton et al., 1998; Grauls and Balaix, 1994]. Excess pore pressures in fine-grained marine strata contribute to marine sediment instabilities and sub-seafloor fluid migration processes [e.g., Dugan and Sheahan, 2012; Taleb et al., 2018]. The generation of sub-seabed excess pore pressures is a consequence of low permeabilities which hinder pore pressure release as the sediments deform under the effect of e.g., rapid burial, glacio-tectonic stress, gravitational slumping, and gas hydrate decomposition [e.g., Locat and Lee, 2002].

It is often assumed that the upper tens of meters of the sediment column is always in hydrostatic equilibrium (i.e., that pore pressures are balanced with the hydrostatic pressure). However, the use of piezometers since the 1970s reveals that pore pressures can be several tens of kPa above hydrostatic pressures in the shallow strata [e.g., Christian et al., 1993; Dugan and Sheahan, 2012; and references therein]. This finding was further developed through numerous piezometer studies for the assessment of sediment stability but also for the understanding of gas hydrate and seepage dynamics at continental margins [e.g., Christian et al., 1993; Dugan and Sheahan, 2012; Sultan and Lafuerza, 2013; Taleb et al., 2018]. There has been a particular focus on quantifying sediment properties in sand dominated settings where hydrates are highly concentrated and have economical potential. However, in-situ measurements for constraining quantitative studies of fluid dynamics and sediment deformation at deep marine (i.e., fine-grained sediment) gas hydrate and seepage systems remains scarce. Gas hydrate formation and destabilization in fine-grained sediment is most often associated with fracture-controlled sub-seabed fluid migration and have therefore implications for slope stability [e.g., Vanneste et al., 2014].

The Vestnesa sedimentary ridge in the eastern Fram Strait consists of fine-grained sediment deposited mostly over oceanic crust [Eiken and Hinz, 1993]. It hosts a gas hydrate and seepage system that extends for > 60 km across the continental rise and slope. Gas migration through near-vertical faults piercing through the gas hydrate stability zone (GHSZ) and seepage, have led to the formation of seafloor depressions known as pockmarks. Among hundreds of pockmarks along the sedimentary ridge, gas bubbles in sonar data are only observed from a few pockmarks on the eastern half of the ridge [Bünz et al., 2012; Hustoft, 2009]. The interpretation of faults and structures along the ridge from gravity maps and seismic data has led to the hypothesis that the evolution of gas seepage along the ridge is closely linked to fault kinematics [Plaza-Faverola et al., 2015]. Tectonic and glacial stress modeling, conducted to test this hypothesis, strongly suggest that temporal and spatial variations in the stress regime along the margin may explain the change in seepage activity through geological time [Plaza-Faverola and Keiding, 2019; Vachon et al., 2022]. Despite a significant number of cross-disciplinary studies about gas hydrate and seepage dynamics in this Arctic region, no in-situ constraints on sediment hydro-mechanical properties were available.

Here we present the first in-situ hydromechanical measurements from the Vestnesa Ridge in the eastern Fram Strait. We integrate piezometer data with geophysical, geotechnical, and sedimentological data, to gain an insight into the petrophysical properties of the sediments that characterize the gas hydrate and seepage system. The study reveals a pattern of spatial variations in sediment stiffness and the presence of localized excess pore pressure layers that are seemingly unrelated to lithology. We discuss the observations in the context of cross-disciplinary evidence for fault-controlled gas seepage in the region. The parameters documented here will help constrain fluid flow and gas hydrate models in the Arctic. More widely, the data and analyses presented here are important for the quantitative understanding of fluid migration, gas hydrate dynamics, sediment stability and seepage phenomena in fine-grained deep marine environments.

2 Geological setting of the Vestnesa Ridge seepage system

Vestnesa Ridge was created by persistent transport of sediment through strong bottom currents (i.e., associated with the West Spitsbergen Current (WSC)) [Eiken and Hinz, 1993]. Spatial changes in seafloor morphology, fault characteristics and seepage evolution lead to the distinction between the eastern and the western Vestnesa Ridge segments [Plaza-Faverola et al., 2015; Schneider et al., 2018; Sztybor and Rasmussen, 2017]. The eastern segment has a narrow (i.e., less than 3 km wide) crest with up to 500 m wide pockmarks aligned along the crest, whilst the western segment is characterized by a > 10 km wide crest where smaller scale pockmarks (100-300 m in diameter) are more randomly distributed. Only 6 pockmarks on the eastern segment release gas bubbles sufficiently large and often to be seen as gas flares in sonar data [e.g., Bünz et al., 2012; Hustoft, 2009; Smith et al., 2014]. Besides evidence from petrophysical, paleontological and geophysical data for the presence of methane in sub-seafloor sediment and the occurrence of major methane seepage events [e.g., Consolaro et al., 2015; Plaza-Faverola et al., 2015; Sultan et al., 2020] methane release through the pockmarks on the western segment has not been detected despite numerous annual surveys.

Seabed pockmarks at the eastern segment are clearly connected to vertical pathways that are in turn associated with sedimentary faults [Plaza-Faverola et al., 2015; Singhroha et al., 2020]. Towards the western segment there is a large variety of sizes and density of fluid escape features and only some of the pockmarks are aligned with fault lineaments at the seafloor [Petersen et al., 2010; Plaza-Faverola et al., 2015]. A well-developed deep marine gas hydrate and associated free gas reservoir exists along the entire Vestnesa Ridge. It is clearly characterized by a continuous bottom simulating reflection (BSR; marking the base of the hydrate zone), high amplitude-low velocity layers and resistivity anomalies, confirming the presence of a free gas column beneath the BSR [Hustoft et al., 2009; Petersen et al., 2010; Goswami et al., 2015; Singhroha et al., 2016; Singhroha et al., 2019; Plaza-Faverola et al., 2017].

Despite uncertainties on the exact location of the continental-oceanic transition (COT) it is known that the Vestnesa Ridge developed dominantly over oceanic crust since the Fram Strait started opening (i.e., 19 Ma ago) [Engen et al., 2008]. The chronology of the ridge is limited to the extrapolation of sedimentary markers from ocean drilling program (ODP) sites on the Yermak Plateau and south of the Molloy transform fault (MTF) [Eiken and Hinz, 1993; Knies et al., 2014; Mattingsdal et al., 2014]. The Miocene succession is poorly constrained. The sedimentary thickness at the eastern Vestnesa Ridge segment is around 5 km [Knies et al., 2018] but the thickness towards the western Vestnesa Ridge segment remains uncertain. Nevertheless, key Plio-Pleistocene time-lines (e.g., indicating the onset of glaciations at c. 2.7 Ma and subsequent glacial intensifications in the region) are well defined along the entire Vestnesa Ridge [Alexandropoulou et al., 2021; Eiken and Hinz, 1993; Knies et al., 2018; Plaza-Faverola et al., 2017]. The youngest late Pleistocene and Holocene sedimentary successions are fairly well constrained from numerous sediment cores analyzed along the margin [Schneider et al., 2018; Sztybor and Rasmussen, 2017].

The accumulation of free gas beneath the GHSZ is sustained by both in-situ microbial gas generation and thermogenic gas that migrated along sedimentary faults [Daszinnies et al., 2021; Hong et al., 2021; Pape et al., 2020; Plaza-Faverola et al., 2017]. High resolution imaging of sedimentary faults has been possible only through the upper 300 m of sediment due to strong seismic attenuation within gas bearing layers beneath the base of the GHSZ along the Vestnesa Ridge crest [Bünz et al., 2012; Singhroha et al., 2016]. The Vestnesa Ridge is situated at the rim of a basin bounded by the oblique spreading Molloy and Knipovich ridges and their associated Spitsbergen and Molloy transform faults (Figure 1). In addition to ridge push forces, the Vestnesa Ridge is subjected to topographically controlled gravitational stress in places and to glacio-tectonic stress due to isostatic adjustment [Vachon et al., 2022].

The piezometer stations were strategically placed to constrain the pore pressure regime at distinct zones along the Vestnesa Ridge and to explore the effect of regional forcing on these pressures (Figure 1): station Pzm4E is at the continental slope near the eastern end of the Vestnesa Ridge; Pzm4W is at the northern rim of a pockmark with active methane release on the eastern Vestnesa Ridge segment; Pzm12E is at the foot wall of a N-S oriented outcropping fault at the transition from the eastern to the western Vestnesa Ridge segments; Pzm12W is at the hanging wall of the same N-S oriented fault; and Pzm5 is just a few kilometers east from the western termination of the Vestnesa Ridge onto the flank of the Molloy Ridge and next to a cluster of seemingly relict pockmarks (Figure 1). Site 5 and 12 are particularly interesting because they are located at the flanks of a sedimentary depocenter which implies enhanced up-dip fluid migration from the free gas zone beneath the base of the GHSZ.

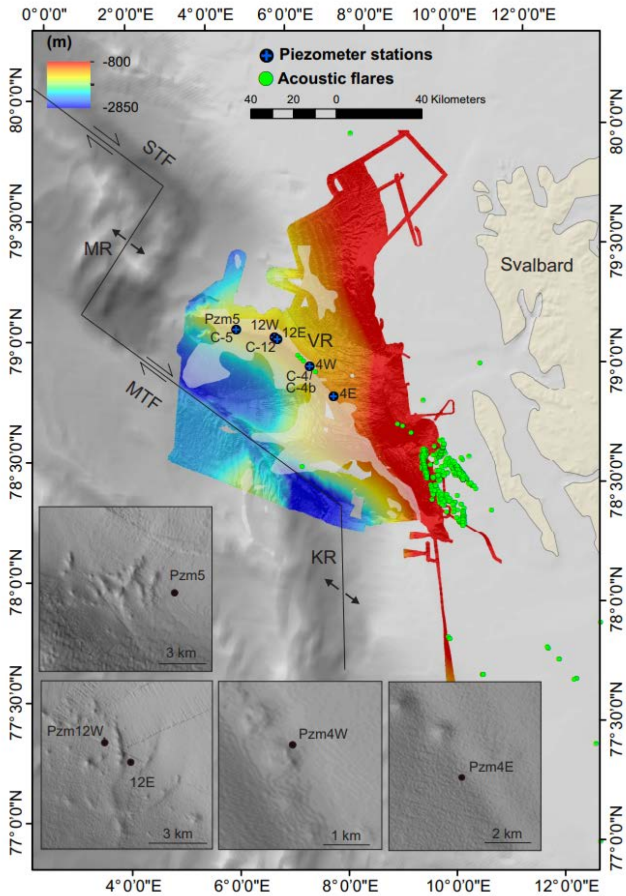

Figure 1: Map of the region showing the piezometer (Pzm) and calypso core (C) transect along Vestnesa Ridge (VR). The piezometer transect extends for about 60 km along the sedimentary drift. The shaded area corresponds to the mapped bottom simulating reflection (BSR). The VR starts north of the Knipovich ridge (KR) termination, and it is bounded by the Spitsbergen Transform Fault (STF) to the north and the Molloy Transform Fault (MTF) to the south. The piezometer (Pzm) sites and calypso cores discussed in this study are from 4 sub-areas along the Vestnesa Ridge.

3 Data and methods

3.1 Geophysical surveying

Piezometer logs as well as petrophysical logs from calypso cores were correlated with chirp data and available high-resolution seismic data. The chirp data were collected with a Kongsberg SBP300 Sub-bottom profiler on board R/V Kronprins Haakon. The maximum penetration is c. 100 m and trace spacing is c. 10 m (vessel speed c. 5 knot and ping rate 4 s). The regional 2D seismic data used for discussing the results in relation to the gas hydrate and free gas system along the Vestnesa Ridge has a spatial resolution of 6.25 m and a vertical resolution of ~5 m at the seafloor [e.g., Plaza-Faverola et al., 2017]. Both chirp and seismic profiles were depth converted using velocity constraints from ocean bottom seismic studies along the ridge [Petersen et al., 2010; Singhroha et al., 2019].

3.2 Calypso core logging, description and lab testing

Calypso cores were taken for correlation with piezometer data using a Calypso Giant Piston Corer operated by the Norwegian Institute for Marine Research and the University of Bergen [Knies and Vadakkepuliyambatta; 2019]; Figure 1; Table 1]. We collected calypso cores at 3 stations along the Vestnesa Ridge (Table 1). Density, P-wave velocity and magnetic susceptibility (MS) logs on the unsplit sections were measured using a multi sensor core logger (MSCL) at UiT – The Arctic University of Norway in Tromsø. Undrained shear strength, S_u, was measured at the base of each section using a pocket torvane with an accuracy of ±0.54 kPa (1 graduation).

Oedometer tests (i.e., a test to study sediment compaction by measuring the deformation/strain of a sample in response to an applied load/stress) were conducted at wholearound sub-samples from 1 depth interval within the upper 7 m along each core using a constant rate of strain (CRS; ASTM, 2006) at the labs by the Norwegian Geotechnical Institute (NGI). In addition, oedometer tests with incremental loading according to the ASTM D-2435 method [ASTM, 2004] were performed on 10 samples at Ifremer at approximately every 2-meter through the upper 9 m of core from superstations 5 and 12. Sediment classification tests (i.e., for water content, grain sizes and plasticity) were conducted on the samples sent to NGI to provide constraints on clay and silt content (2–63 μm) (Table 1).

The open cores were visually logged and scanned with an Avaatech XRF core scan for high-resolution digital photographs. The upper 9 m of the calypso cores were subsampled in 1-cm thick slices at 10 cm intervals in cores C-4 and C-12. Core C-5 was subsampled every 20 cm, except between 4 to 5 m depth where the sampling was performed every 10 cm (i.e., this core is being primarily used for other studies within paleo-oceanography). The textural characteristics of the sediments were determined through wet sieving at 63 μm to separate the mud fraction (clay and silt) from the fractions coarser than 63 microns (sand, gravel and pebbles) (Figure 2).

Table 1. List of samples from calypso cores available for the study. BWT=bottom water temperatures [Knies and Vadakkepuliyambatta, 2019; Plaza-Faverola, 2020]; BSR=bottom simulating reflection [Plaza-Faverola et al., 2017].

Calypso core site	Site number (super stations)	Core ID	Lat	Long	Water depth (m)	BWT C°	BSR depth (mbsf)	Sample depth (m)
CAGE19-3-KH-04	4	C-4	78.9967	6.9635	1194	-0.15	190.00	6.13
CAGE19-3-KH-12	12	C-12	79.1285	6.1285	1234	-0.40	170.00	6.60
CAGE19-3-KH-05	5	C-5	79.1427	5.2749	1321	-0.70	160	5.41

3.3 Piezometer data acquisition and processing

In-situ excess pore pressure (P) and temperature (T) were measured at 5 stations (Table 2) between water depths of ~1120 and ~1330 m along the Vestnesa Ridge (Figure 1). The measurements were done using the Ifremer piezometer [Sultan et al., 2010] which consists of a sediment lance of 60 mm diameter that carries sensors for measuring pressures exceeding the hydrostatic pressure (i.e., excess pore pressures) and temperatures. Differential pore pressure sensors are mounted in the piezometer with an outer membrane subjected to the sediment pore pressure and inner membrane exposed to the hydrostatic pressure. In this way, the sensors are not sensitive to the hydrostatic pressure and water depths. Pressure sensors are zeroed before penetration in the sediment.

The lance was ballasted with lead weights (up to 1000 kg), was driven to the seafloor from the rear of the ship with a Dyneema ® cable (strong rope) and it was left on the seafloor to record autonomously from the ship for 2-4 days. The lance penetrated 8-9 m in soft clayey material (Table 2). The recovery was done through a rope attached to a surface buoy. The piezometer pressure and temperature sensors have an accuracy of ±0.5 kPa and 0.05 °C, respectively.

Table 2. Summary of Piezometer stations. The data were collected during two scientific expeditions on board R/V Kronprins Haakon (Knies and Vadakkepuliyambatta, 2019; Plaza-Faverola et al., 2020). From west to east the piezometer (Pzm) stations are named 5, 12W, 12E, 4W and 4E. The numbers correspond to super stations where Calypso cores were also recovered in the 2019 expedition.

Simplified name	**Station name**	**Number of sensors**	**Penetration depth (m)**	**Coordinates**	**Water depth (m)**	**Recording period (Time UTC)**
Pzm5	KH19-05-PZM2	9 P and 9 T	9.92	79.143 N–5.274 E	1330	26/10/2019 - 12:11 31/10/2019 - 2:08
Pzm12W	KH20-12-PZM1	8 P and 9 T	8.64	79.120 N-6.1348E	1234	20/10/2020 18:22 23/10/2020 19:52
Pzm12E	KH20-12-PZM2	8 P and 9 T	8.64	79.11245N-6.201733E	1228	23/10/2020 23:00 27/10/2020 10:17
Pzm4W	KH20-04-PZM1	8 P and 9 T	8.64	79.00475N-6.9353E	1207	21/10/2020 19:45 24/10/2020 19:09
Pzm4E	KH20-04-PZM2	8 P and 9 T	8.64	78.88152N-7.4766E	1127	25/10/2020 02:06 27/10/2020 18:46

Immediately after penetration of the sediment by the piezometer, pore pressures and temperatures peak, followed by a progressive decay towards equilibrium. These initial data peaks are due to the compression and shear of surrounding sediment under undrained conditions [Burns and Mayne, 2002]. Generally, it takes a few hours for the temperature to reach the equilibrium. The equilibrium temperatures are used in this study to determine the thermal gradients at the piezometer locations.

For sites with low-permeability sediment, long-term dissipation tests (several weeks) are needed to reach in situ equilibrium pore-water pressure (Δu_{eq}), which would be hardly affordable for offshore operations. Consequently, short-term/partial dissipation tests are usually performed and Δu_{eq} is predicted from partial measurements. For our analyses, we used a cavity expansion approach [Sultan and Lafuerza, 2013] to simulate the pore water dissipation process after the piezometer deployment. The differential equations and numerical method used in this approach are detailed in the supplemental material (Supplement Text S3). The dissipation curve depends on the hydro-mechanical properties of the sediment and is mainly modulated by the hydraulic diffusivity (C_h) and the rigidity index (I_r) through the ratio $\frac{C_h}{\sqrt{I_r}}$. The dissipation curve is also affected by the initial excess pore pressure generated after the piezometer installation (Δu_i) which was shown to be strongly dependent on the stiffness and the undrained shear strength (or undrained cohesion), S_u, of the affected sediments [Burns and Mayne, 1998]. In this study, we use the pore pressure dissipation tests to derive $\frac{C_h}{\sqrt{I_r}}$ and Δu_{eq}. The Δu_i is obtained directly from the piezometer pore-pressure data and is used as an indicator of the stiffness of the sediment.

4 Results

4.1 Sedimentological properties

The sediment cores recovered a lithostratigraphic sequence already well described in other areas in the eastern Fram Strait. They show a consistent pattern in magnetic susceptibility (MS), lithology, and color of the sediments as described in 11 cores from the western Svalbard margin spanning the last 30 ky [Jessen et al., 2010]: a dark unsorted layer of low MS consisting of coarse material of black and brown shales dating 24 ka and a laminated clay layer of low MS dating c. 15 ky (Figure 2). The pattern of MS typical for the western margin has later been shown to be consistent both at Vestnesa Ridge [e.g., Howe et al., 2008; Consolaro et al., 2015; Sztybor and Rasmussen, 2017], southwest of Svalbard [Lucchi et al., 2013; Lucchi et al., 2015; Caricchi et al., 2019] and north of Svalbard [Chauhan et al., 2016]. The event Meltwater Pulse MWP-1A documented in [e.g., Lucchi et al., 2013] is also recognized as dark, finely laminated sediments of low MS. The recognition of these stratigraphically well-constrained and wide-spread marker-beds associated with major paleo-climatic events, were used as a base to constrain the age models and to correlate the sediment cores. Further correlation refinements based on the MS trend show the following main paleo-climatic events in cores C-4, C-12 and C-5 (Figure 2): the cold 8.2 ky event, the 29 ky MIS 3–2 boundary, and the 60–57 ky event (Heinrich event H6; inferred in core C-4).

The sediment sequences at Vestnesa Ridge thus consist of alternating bioturbated fine-grained and ice rafted debris (IRD) rich deposits associated with bottom current transport and iceberg release of detritus, respectively; and laminated sediments coupled with massive IRD intervals associated with deglaciations at the MIS 4–3 and MIS 2–1 transitions [e.g., Caricchi et al., 2019; Consolaro et al., 2015; Jessen et al., 2010; Jessen and Rasmussen, 2015; Lucchi et al., 2013; Lucchi et al., 2015; Sztybor and Rasmussen, 2017] (Figure 2).

The correlation among cores outlined generally increasing sedimentation rates as we move westwards from the location of core C-4 towards the location of core C-5 with the exception of the stratigraphic interval located between the base of the laminated layer and the base of the 24 ky event, corresponding to the Late Weichselian glaciation, during which the sedimentation rate increased eastwards (i.e., proximal source of glacigenic sediments) (Figure 2).

Piezometer station Pzm4W is a few meters west from C-4 (Figure 1). One aspect we find in the literature that makes this area different from the other sites (Pzm5, Pzm12W, Pzm12E, Pzm4E) is the lack of the Holocene time interval in sediment cores, linked to patterns of non-deposition by the west-Spitsbergen bottom currents [Elverhøi et al., 1995; Howe et al., 2008; Jessen et al., 2010; Schneider et al., 2018; Sztybor and Rasmussen, 2017]. Fewer stratigraphic studies have been conducted as we move westward along the Vestnesa Ridge. However, the upper 5–6 m of sediments are generally described in the literature as dominantly silty-clayey hemipelagic deposits with intervals characterized by laminations, and dropstones at time intervals that correspond to key glacial events (e.g., the last glacial maximum LGM) [Schneider et al., 2018; Sztybor and Rasmussen, 2017].

The grain size analyses available from the 3 Calypso cores also indicate that the upper 9 m of sediment are dominantly silty clay (i.e., > 80 % grain sizes < 63 µ) along the 40 km transect between these three sites (Figure 2). The distribution of the grain size fraction > 63 µm, is mostly associated with the presence of IRD and glacigenic sediment input from the shelf. Despite the proximal location of site C-4 to the continental shelf compared to site C-5 (i.e., proximal to the mid-ocean ridge) (Figure 1), the content of fraction > 63 µm does not show a progressive spatial change along the three sampled sites (Figure 2). Intervals with > 10 % coarser sediment (> 63 µm) are present at various depths at all the sites, indicating that there is not a progressive trend of grain size decrease as the Vestnesa Ridge gets deeper.

Bulk wet density logs obtained from MSCL logging of the three cores C-4, C-12 and C-5 show a slight westward decrease in density from being around 1.5 g/cm^3 at C-4 and as low as 1.2 g/cm^3 at C-5 within the upper 3 meters. This is directly reflected on the calculation of effective stress assuming hydrostatic equilibrium along the Vestnesa Ridge. This upper 3 m interval at C-5 is also characterized by anomalously low P-wave velocities from the MSCL (i.e., as low as 1300 m/s), suggesting increased void space (e.g., cracks) or the presence of gas within the sediment pores. Average P-wave velocities also show a very gentle westward decrease between 1500–1550 m/s.

Other deeper intervals (e.g., between 5 and 15 m in cores C-5 and C-12) show velocities as low as 1200 m/s (Supplement - Figures S6-8).

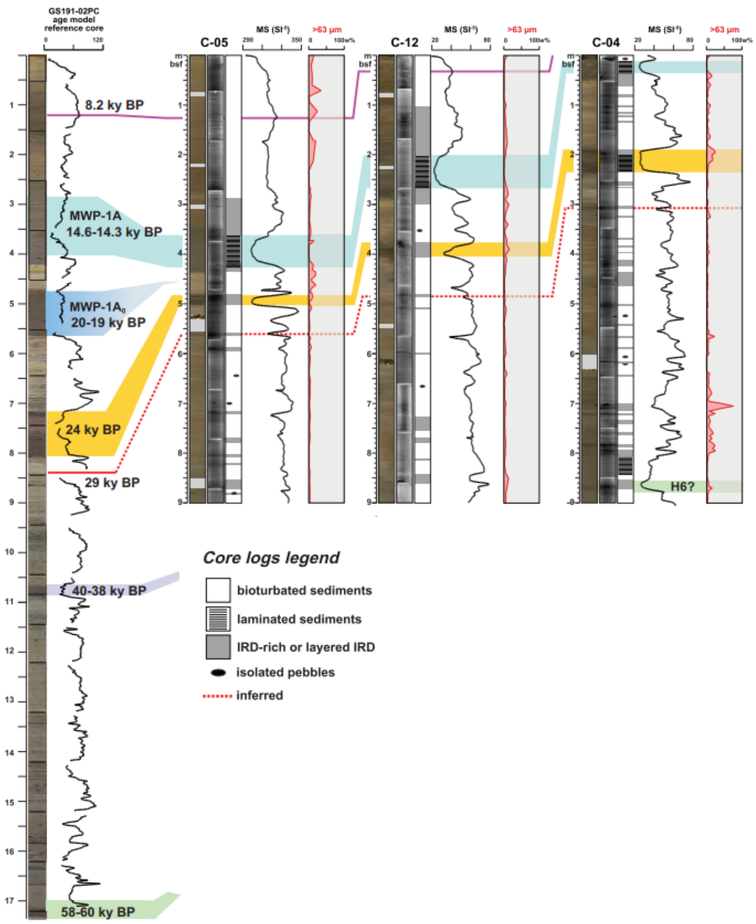

Figure 2: Sedimentological logs (photos, radiographs and synthetic lithological log), magnetic susceptibility (MS), and grain size distribution (> and < 63 microns) along the upper 9 m of the calypso cores from stations 05, 12 and 04 (from west to east). An additional core from the Bellsund Drift (south east from the VR) is included to support the chronostratigraphy and to highlight the regionality of the correlation. Major paleo-climatic events have been correlated based on documented multi-proxies analyses from the region [Caricchi et al., 2019; Jessen and Rasmussen, 2019; Jessen et al., 2010; Lucchi et al., 2013; Schneider et al., 2018; Sztybor and Rasmussen, 2017].

4.2 Geotechnical constraints

The geotechnical parameters obtained from the oedometer tests (CRS and incremental loading) and the index tests are presented in Table 3 (Supplement figures S1-S5). The plasticity index (Ip) determined from six samples (Table 3) did not show any important change among the samples (except for sample C-12 at 14.59 mbsf). While the percentage of clay (grain sizes < 2 µm) measured at the lab shows a westward increase from 32–49 % at C-4 to 54–64 % at C-5, the I_p doesn't reflect any significant westward trend (Table 3). It is important to notice that the depth of the samples from different cores does not correspond to the same chronological interval.

The vertical hydraulic diffusivities determined at the in-situ effective stress conditions (C_{v0}) from oedometer tests indicate that there are no westward changes when moving from C-4 to C-5.

However, an important vertical fluctuation can be observed at C-5 and C-12. The compressibility indices (Cc) derived from the incremental and CRS oedometer tests are shown in Table 3 (Supplement figures S3-S5) and indicate once again no trend from west to east (C-5 versus C-12 in Table 3) but a decrease in Cc was observed with increasing depth (Table 3). This trend is well marked through the upper 2 m of sediments.

Table 3. Summary of geotechnical data obtained from oedometer (CRS and incremental loading) and index tests.

Core	Depth (m)	Ip	Clay content (%)	C_{v0} (x10^{-7} m^2/s)	Cc	Oedometer test
C-5	5.41	41	64	0.2	0.55	CRS
C-5	16.28	44	54	0.4	0.63	
C-12	6.60	42	58	0.4	0.47	
C-12	14.59	21	59	0.4	0.50	
C-4	6.13	42	49	0.4	0.67	
C-4	14.00	42	32	0.3	0.53	
C-5	0.80	-	-	0.14	1.04	Incremental loading
C-5	2.30	-	-	0.18	0.90	
C-5	3.10	-	-	0.07	0.61	
C-5	5.50	-	-	0.09	0.47	
C-5	8.60	-	-	0.15	0.59	
C-5	9.40	-	-	0.19	0.44	
C-12	0.84	-	-	0.02	0.80	
C-12	2.30	-	-	0.07	0.58	
C-12	5.50	-	-	0.05	0.45	
C-12	9.40	-	-	0.40	0.36	

4.3 In-situ piezometer measurements

Temperatures measured around 0.5 m above the seabed at sites Pzm12W, Pzm12E, Pzm4W and Pzm4E (Figure 3) are almost constant throughout the monitoring period, except for small disturbances at discrete intervals and periods (Figure 3). The temperature within the sediments decayed to reach the in-situ equilibrium temperature in approximately 4 to 6 hours (Figure 3).

Despite the relative long monitoring period (2.7 to 4.6 days), most of the pressure dissipation curves did not reach the equilibrium pressure (Δu_{eq}). The low hydraulic diffusivity of the sediment seems to prevent a fast dissipation of the induced pore pressure. Nevertheless, for the majority of the curves, the dissipation was in a sufficiently advanced state to allow a derivation of Δu_{eq} by using the cavity expansion approach (Supplement figures S9-S13).

Temperature gradients as well as hydro-mechanical properties (i.e., hydraulic diffusivity, maximum penetration pressure, equilibrium pressure) were derived from sensor data at the 5 piezometer stations (Figure 4). These properties allow constraining sediment stiffness and the degree of excess pore pressures along the Vestnesa Ridge.

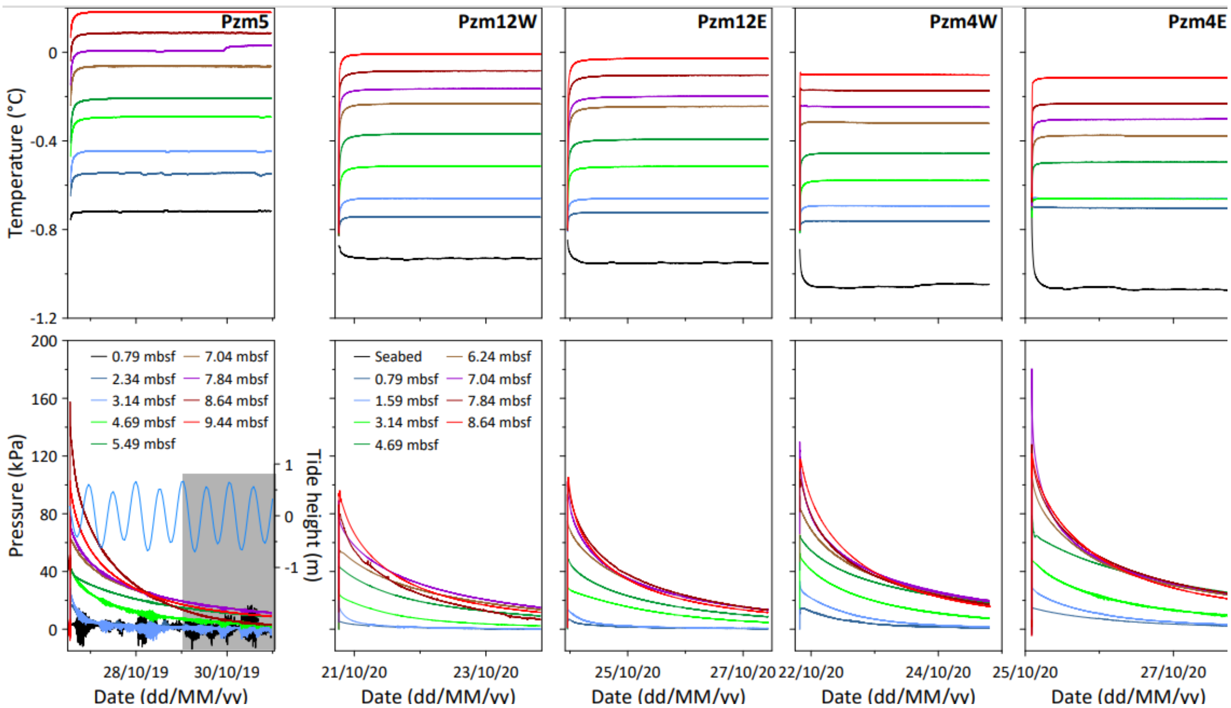

Figure 3: Sensor data from piezometer sites (from west to east): Pzm5, Pzm12W, Pzm12E, Pzm4W and Pzm4E. The plots show temperature and pore pressure versus time. The data from Pzm5 is discussed in [Sultan et al., 2020]. The different colors indicate the sensor depths below the seabed. Sensor depths are between 0.79 mbsf (blue curve) and 9.44 mbsf (red curve) for Pzm5 and between 0.79 mbsf (blue curve) and 8.64 mbsf (red curve) for the rest of the stations. The figure legend for Pzm12E, Pzm4W and Pzm4E is similar to the legend of Pzm12W. The dashed area indicates the data shown in Figure S15.

4.3.1 Thermal gradients

The in-situ temperatures (T_{situ}) were calculated as an average of temperature values recorded 24 hours after the piezometer installation. The thermal gradients were calculated from the linear part of the T_{situ}-depth data (Figure 4a) and they show a gradual westward increase from 85°C/km at site Pzm4E to 98°C/km at site Pzm5 (Figure 4a). This is consistent with the reported increase in geothermal gradient as the sedimentary basin approaches the Molloy Ridge [e.g., Crane et al., 1988]. The deviation of the temperature recorded by the shallowest sensors from the linear thermal gradients (Figure 4a) could be explained by local seabed temperature changes.

4.3.2 Hydro-mechanical properties

Hydraulic diffusivity

The pressure data suggest that the hydraulic diffusivities ($\frac{c_h}{\sqrt{I_r}}$) do not evolve monotonically with depth. For instance, for site Pzm12W (Figure 3), the excess pore pressure recorded by the two deepest sensors (at 7.84 and 8.64 mbsf) showed a faster decay with respect to the two shallowest sensors (7.04 and 6.24 mbsf). The same phenomenon can be also observed on some of the other sites (Figure 3).

Maximum pressure after penetration

The maximum pore pressure after penetration (Δu_i) generally increases with depth for a given lithology under a classical evolution regime of sediment stiffness [Burns and Mayne, 2002]. The Δu_i versus depth profiles, for the 5 studied sites, shows no linear increase with depth as is usually expected for normally consolidated homogeneous soils [Skempton, 1964; Velde, 1996]. For instance, at sites Pzm5 and Pzm4W (Figure 3), the highest Δu_i values were measured at 8.64 mbsf and 7.04 mbsf respectively, and not at the level of the deepest sensors (9.44 mbsf for Pzm5 and 8.64 mbsf for Pzm4W). The background Δu_i increases progressively with depth (i.e., with values between 7 and 78 kPa at the westernmost site Pzm5 and reaching values between 14 and 128 kPa at the easternmost station Pzm4E; Figure 3). However, between 6 and 8 mbsf, Δu_i increase abruptly for all the sites (i.e., reaching values of up to 180 kPa at the easternmost station, Pzm4E). This anomalous evolution of Δu_i is more accentuated for site Pzm5. Here, the data show a decrease of Δu_i between 4 and 5 mbsf (i.e., significantly lower than at other sites) and a sudden increase between 8 and 9 mbsf (Figure 4d). Sites Pzm12W and Pzm12E (Figure 4d) confirm the non-linear trend with a sudden change in Δui-depth slope between 6 and 7.5 mbsf.

The undrained shear strength measured using the torvane shows a similar trend in the S_u-depth profile (Figure 4e). The undrained shear strength profile acquired from core C-12 shows that Δu_i and S_u follow the same trend (Figure 4e). For the two sites, Pzm4W and Pzm4E, the Δu_i-depth slope changes again between 6 and 7.5 mbsf. The plasticity index values obtained for all the sites at one sample at c. 6 mbsf are included for comparison (Figure 4c). The small range of variation in I_p for all the sites (41–42) suggest that, at least at the depth of the samples, there are no significant lateral changes in the clay plasticity along the 60 km long transect.

Finally, pore pressure dissipation was locally disturbed by sudden variations in pressure at certain sites, particularly at sites Pzm5 and Pzm12w (Figure 4). In agreement with observations from other piezometer studies, this mainly corresponds to the presence of free gas partially saturating the sediment, which makes the pore pressure regime sensitive to tidal cycles [e.g., Sultan et al., 2020].

Equilibrium pressure

The Δu_{eq} was calculated for 35 piezometer P-sensors (Supplement – Figures S9-S13). For each set of pressure-data, Δu_{eq} values were retrieved after three runs (Figure 4b). Only piezometers Pzm12W and Pzm12E showed excess pore pressures beyond the instrumental resolution and method uncertainties (i.e., overpressures between 5 and 15 kPa; Figure 4d). Between 5–10 mbsf Pzm4w and Pzm5 show excess pore pressures just under c. 2.5 kPa (Figure 4d) that should be interpreted with caution because these are within the experimental and calculation errors. The pressure dissipation function $\frac{C_h}{\sqrt{I_r}}$ is primarily influenced by the hydraulic diffusivity (i.e., directly proportional to C_h) and to a lesser degree by the stiffness of the sediment (inversely proportional to the square root of the plasticity index I_r). $\frac{C_h}{\sqrt{I_r}}$ values vary slightly, between 10^{-8} and 10^{-7} m^2/s for sites Pzm5, Pzm4E and Pzm4W (Figure 4c). However, $\frac{C_h}{\sqrt{I_r}}$ values for Pzm12W and Pzm12E vary significantly with depth, with calculated values between 10^{-10} and 10^{-6} m²/s (Figure 4c). The lowest dissipation ratio correlates well with the highest Δu_{eq} (Figure 4b and c) at site Pzm12W. Oedometer tests (CRS and incremental loading) were used to determine the vertical hydraulic diffusivities (C_{v0}) at the estimated in-situ effective stress (σ'_{v0}) at hydrostatic equilibrium. Although the comparison between C_h and C_{v0} is not accurate due to the difference in dissipation conditions between the laboratory (i.e., vertical dissipation through disturbed samples) and in situ measurements (i.e., mostly horizontally through intact sediments), a qualitative comparison shows consistency between the two trends ($\frac{C_h}{\sqrt{I_r}}$ versus depth and C_{v0} versus depth). For instance, oedometer tests confirm that vertical hydraulic diffusivities barely vary with depth for sites Pzm5, Pzm4E and Pzm4W (Figure 4c) whilst an important change in C_{v0} with depth is observed at sites Pzm12W and Pzm12E (Figure 4c).

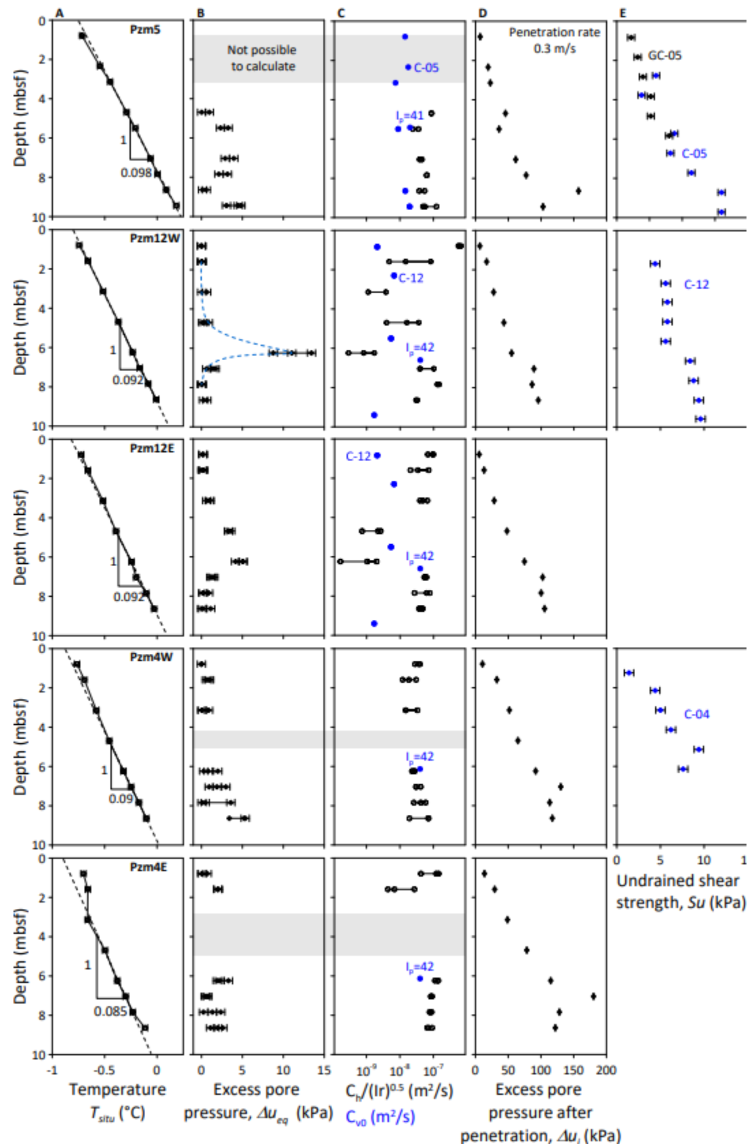

Figure 4: Thermal gradient and hydro-mechanical properties (vertically from west to east): Pzm5, Pzm12W, Pzm12E, Pzm4W and Pzm4E. a) Temperature at equilibrium versus depth are used to calculate the in-situ thermal gradient. b) Equilibrium pore pressure Δu_{eq} and c) $\frac{C_h}{\sqrt{I_r}}$ are derived by modeling the pore pressure decay curve (Supplement – Figures S9-S13). d) Pore pressure after penetration (Δu_i) is obtained from the in-situ pore pressure measurements.

Geotechnical properties including the hydraulic diffusivity (C_{v0}), the plasticity index (I_p) and e) the undrained shear strength (S_u) are obtained from laboratory testing. Grey dashed areas correspond to sensors where the calculation of the Δu_{eq} and $\frac{C_h}{\sqrt{I_r}}$ was not possible to achieve. The penetration rate of the 5 piezometers was approximately 0.3 m/s. T, P and Su sensor accuracies are shown as error bars. The lower and upper limits of the parameters ($\frac{C_h}{\sqrt{I_r}}$ and Δu_{eq}) derived from the piezometer measurements are also indicated.

5 Discussion

The in-situ pressure and temperature data as well as the sedimentological and geotechnical analyses lead to several main observations concerning the hydro-mechanical properties of the upper sedimentary layers along the Vestnesa Ridge. We discuss the processes that reconcile cross-disciplinary results from the area and the implications that the newly documented data have for the understanding of gas transport and sub-seabed deformation of fine-grained sedimentary systems.

5.1 Spatial variations in sub-seabed sediment stiffness

A combination of in-situ pore pressure measurements and geotechnical lab measurements confirmed that the stiffness of the sediment can be inferred from Δu_i [Burns and Mayne, 2002; Sultan and Lafuerza, 2013]. By comparing Δu_i to measured S_u at sites Pzm5, Pzm12W and Pzm4W, the data show a link between the maximum pressure generated during lance penetration and the undrained shear strengths of the sediment (Figure 4) allowing us to infer variations in sediment stiffness.

A change in sediment stiffness in the vertical profiles is inferred from a non-progressive increase in Δu_i evident from all the piezometer stations between 5-9 m (e.g., Δu_i increases from 48.64 kPa at 4.69 m to 75.01 at 6.24 m for Pzm12E; Figure 5b), together with a faster increase in S_u from around 6 m (most evident from Pzm5 and Pzm12E data; Figure 4e).

Sediment stiffness seems to change also spatially, decreasing westwards along the Vestnesa Ridge (i.e., Δu_i decreases progressively from Pzm4E to Pzm5; Figure 5b). The undrained shear strength data is less robust and not available for all the sites. However, a relative westward decrease is also evident through the upper 5 m by comparing values for cores C-4, C-12 and C-5 (Figure 4e). Calculated effective stress assuming hydrostatic equilibrium conditions (σ'_{v0}) (Supplement – Figures S1 and S2) also shows a westward decrease (e.g., σ'_{v0} at 10 mbsf is c. 42 kPa at the location of C-4 and c. 37 kPa at C-5; Figure 5c). This is not surprising because sediment densities from the calypso cores (i.e., used for the calculation) decrease westward. What is interesting from this calculation is that the relative westward decrease in σ'_{v0} (around 11%) is not comparable to the decrease in sediment stiffness (i.e., inferred from Δu_i values) from the eastern to the westernmost piezometer stations, which can be > 200% at discrete sedimentary intervals (e.g., at c. 7 m; Figure 5b). This suggests that we are facing a process that is slightly modifying the γ-density (i.e., decreasing the effective stress under hydrostatic equilibrium progressively towards the mid-ocean ridge) and that is simultaneously changing more drastically the structure and the strength of the sediment (Figure 5d).

Hereafter we discuss the processes that may explain the inferred spatial variations in sediment stiffness and measured decrease in sediment densities.

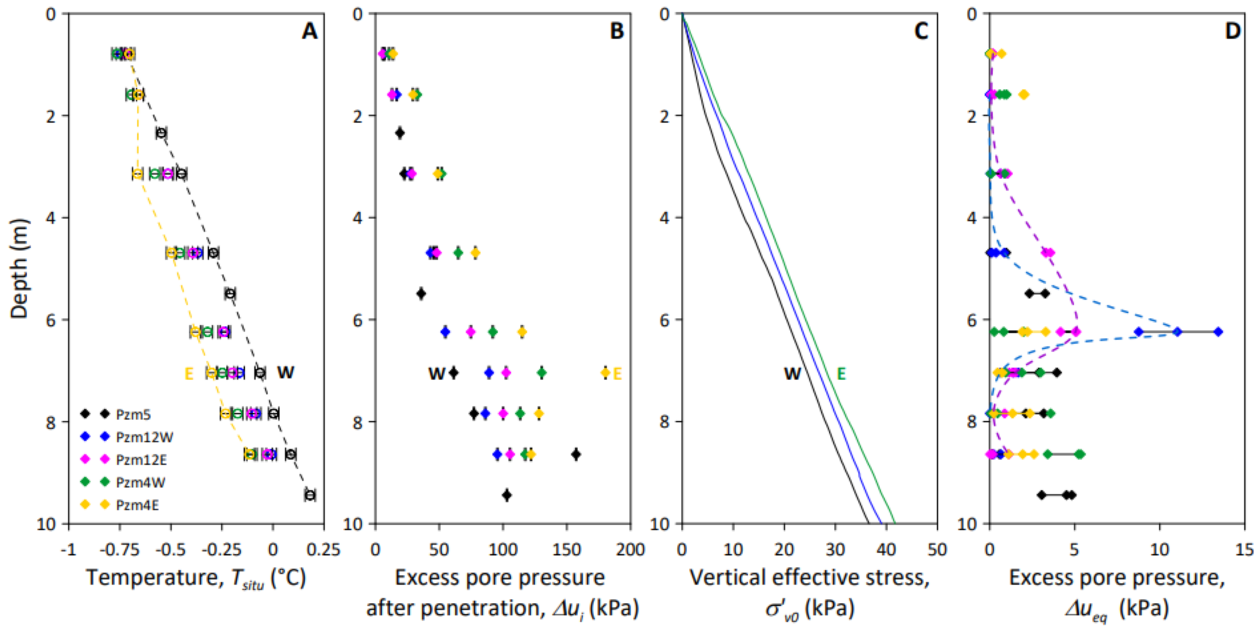

Figure 5: Summary of pore-pressure and temperature data for all the piezometer stations. a) Temperature and b) Δu_i versus depth derived from the piezometer sensor data. c) Vertical effective stress (σ'_{v0}) versus depth assuming hydrostatic conditions, estimated from the measured γ-density on calypso cores (C-5, C-12 and C-4 in Figure 1). d) Δu_{eq} versus depth obtained by back calculation using the piezometer pore-pressure sensor data. T and P sensor accuracies are shown as error bars. The lower and upper limits of the Δu_{eq} derived from the piezometer measurements are also indicated.

5.2 Possible processes affecting sediment stiffness

5.2.1 Lithology and consolidation state

For a homogeneous and normally consolidated sediment, the stiffness is expected to increase linearly with depth [Skempton, 1957]. The data do not indicate a linear and homogeneous increase in sediment stiffness, but rather abrupt vertical changes and a trend of stiffness decrease as the Vestnesa Ridge gets deeper. A decrease in stiffness could be controlled by a change either in lithology or in the consolidation history. In a sedimentary setting with an input exclusively from the shelf, the sediment particles would become progressively finer at more distal areas from the shelf. However, the analyses of cores along the Vestnesa Ridge do not show a progressive decrease in grain sizes as the ridge gets deeper (i.e., the sediments are > 80% silt and clay, with a slight westward increase in clay, with sporadic intervals characterized by 10–20% coarser grains associated with major climatic events of ice-rafting; Figure 2).

The cores show that the Vestnesa Ridge predominantly receives sediments transported by the WSC that enters deeper waters and forms depocenters. These depocenters shift spatially on glacial-interglacial time scales. During ice sheet advance and retreat sediment depocenters move closer to the ice terminus on the continental margin (site 4) although coarser glacigenic material has been deposited all along the ridge, reaching also site 5, closer to the mid-ocean ridge. This, together with a random input of sediments (i.e., IRD) from icebergs [Eiken and Hinz, 1993; Nielsen et al., 2007], breaks the pattern of progressive more distal decrease in grain size along the Vestnesa Ridge (Figure 2). During the last interglacial (i.e., the Holocene) the sedimentation is mainly driven by the deep component of the WSC shifting the depocenter to the deeper part of the Vestnesa Ridge (site 5), generating expanded sequences characterized by low density. The proximal, shallower area (C-4) is affected by the more vigorous, shallow component of the WSC causing sediment by-pass or substrate erosion responsible for condensed sequences or the lack of the Holocene record.

The stratigraphic correlation across all the sites with the chirp data show that the apparent lack of Holocene affects primarily the pockmark area where Pzm4W is located and to some extent the area around Pzm4E (Figure 6). Piezometer Pzm4W penetrated the oldest sediment. This implies that the trend of westward decrease in stiffness picked up by the Piezometer is not associated with a progressive westward change in clay content within the same depositional time span. Also, despite this age difference in the otherwise continuous chrono-stratigraphic transect, a significant change in lithology along the ridge is not evident from the (limited) plasticity index values from lab tests (Figure 4c) nor from grain size analyses. Thus, the stratigraphic information and geotechnical data does not support a lithological explanation for the westward progressive decrease in stiffness and for an abrupt change in stiffness vertically.

ODP global data show that compaction in clayey sediments in deep marine environments within the upper 500 m is not controlled by sediment age [Velde, 1996]. This means that there is no dominant chemical or diagenetic compaction, but that physical compaction dominates (i.e., namely by the accommodation of grains upon deposition by bottom currents in the case of this Arctic setting). Moreover, background in-situ pore pressure data show hydrostatic conditions (Δu_{eq}=0 or within the instrumental and calculation errors of ±2.5 kPa) for almost all the P-sensors (i.e., except for two sensor depths at Pzm12W and Pzm12E - Figure 5c), indicating that the penetrated sediment is dominantly normally or over-consolidated along the entire transect. However, the undrained shear strength (S_u) profiles (Figure 4) show the absence of a gradient over the upper 6 m, pointing towards a disturbed rather than over-consolidated sedimentary interval.

Among the factors influencing compaction (e.g., sedimentation rate, sediment structure and type of clay) we think that changes in the sediment structures explain the pressures obtained upon piezometer penetration. The inferred westward decrease in sediment stiffness through the upper 6 meters along the ridge (Figure 4 and Figure 5b) is associated with a process that is affecting in particular the western Vestnesa Ridge segment.

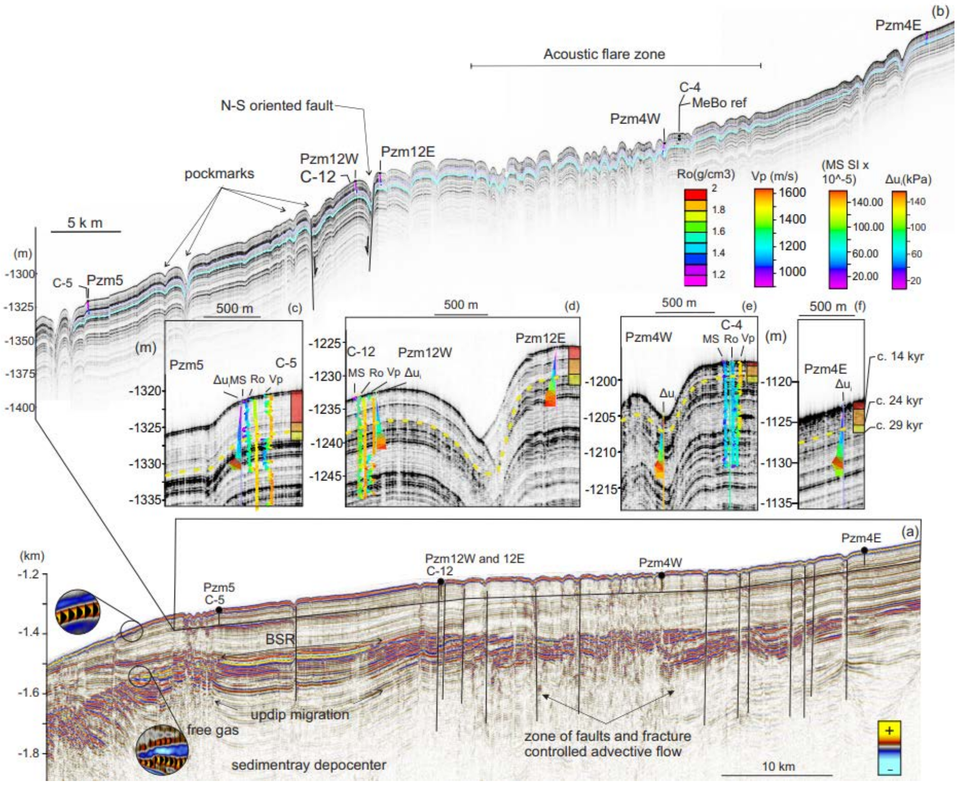

Figure 6: a) Same depth converted seismic profile as in Plaza-Faverola et al., [2017] putting piezometer and core data in the context of the regional gas hydrate system along the Vestnesa Ridge in the Fram Strait. BSR= bottom simulating reflection; b) Overview of the spatial distribution of Calypso cores (C-05, 12 and 04) and piezometer sites (Pzm05, 12W, 12E, 4W, 4E) over a chirp profile. Chirp data were depth converted using available interval P-wave velocity information from ocean bottom seismic investigations in the area [Singhroha et al., 2019].

5.2.2 Gas-hydrate distribution and dissolution

The spatial variation in the thickness of the GHSZ along the Vestnesa Ridge makes us reflect on the effect of the thermal regime from mid-ocean ridge spreading on gas transport and hydrate stability. The increase in the geothermal gradient as the sedimentary ridge approaches the Molloy Ridge results in a temperature-controlled decrease in the GHSZ (i.e., the BSR gets shallower from c. 200 mbsf at site 4 to c. 160 mbsf at the westernmost end of the BSR despite the increase in water depth [Plaza-Faverola et al., 2017]). All the piezometer sites (Figure 5a) registered this thermal effect (i.e., consistent with regional heat flow measurements by Crane et al., [1988]). Gas hydrate samples have previously been retrieved exclusively from the upper 2-4 m in sediment cores taken from active seepage pits. These samples show that hydrates form in thin flake-like layers in small fractures or as cm scale gas nodules [e.g., Panieri et al., 2017; Sultan et al., 2020].

A westward decrease in gas-hydrate saturation could explain the inferred decrease in sediment stiffness [Lei and Santamarina, 2019; Taleb et al., 2018; Waite et al., 2009; Yoneda et al., 2017]. Alternatively, it could be the process of hydrate decomposition rather than the relative decrease in gas hydrate concentrations that is affecting the stiffness and the undrained cohesion of the host sediments. Hydrate decomposition may take place by dissolution [Zhang and Xu, 2003] within the GHSZ if it is the result of chemical instability (e.g., low methane concentration in the surrounding seawater). In this case, gas hydrate becomes a mixture of water and dissolved gas and is expected to alter the stiffness and the undrained cohesion of the host sediments [Sultan, 2007]. The gas-hydrate dissolution process may explain the observed degradation of the stiffness of the host sediment as we move westward along the Vestnesa Ridge. This implies a stop or decrease in the input of gas into the system towards the western part of the ridge at a given period of time, to cause such a dissolution. However, this process does not explain why the surface sediment (<6 mbsf) is the most impacted. Dissolution is expected to alter the sediments regardless the effective stress and therefore the depth within the sedimentary column. Nonetheless, it is not possible to infer a pattern of spatial distribution of hydrates from the pore pressure sensor data (mainly Δu_i) and the cores; no evidence of gas hydrates within the investigated depths (i.e., gas hydrate layers would yield Δu_i values well above the ones reported here [Taleb et al., 2018]).

5.2.3 Free gas expansion and exsolution

Another process that is well known to affect the stiffness and undrained cohesion of clayey sediments is the persistent input of gassy fluids into the porous medium. Several authors have already shown how a few percent of gas saturation is enough to damage the sediment structure and highly affect its shear strength with little effect on its density [Hight and Leroueil, 2003; Lunne et al.; Sultan et al., 2012; Wheeler, 1988; Zhu et al., 2021]. Sultan et al. [2012] showed that the effect of gas expansion is more pronounced at low mean effective stress (i.e., within the upper sediments) and their experimental data on plastic fine-grained sediment demonstrate that the presence of free gas in the upper shallow soft sediment may alter its shear strength significantly. The change in behavior observed from above and below the 6-7 m depth interval may correspond to a threshold in the effective stress at hydrostatic condition (25 to 35 kPa) where the free-gas expansion and compression can alter the structure of the sediment.

The westward decrease in the GHSZ thickness has implications for the rate of gas diffusion from the free gas zone beneath the BSR towards the seafloor. For a given gas concentration in the free gas zone, more dissolved gas will reach the seabed via diffusion at shallower BSR depths and higher temperatures (Figure 7). The methane solubility at the BSR level at both sites Pzm5 and Pzm4W is expected to be between 123 and 126 mM (Supplement - Figure S14). The solubility was calculated using the approach by Spivey et al. [2004] for the temperature and pressure conditions at the base of the BSR (Supplement – Figure S14). For Pzm5 (depth=170 mbsf; T= -1.05°C; salinity= 34.5 g/L), the methane solubility would be 123 mM while for Pzm4w, (depth=200 mbsf; T= -0.95°C; salinity= 34.5 g/L), the methane solubility would be 126 mM. Assuming a permanent diffusion regime and dissolved methane concentrations lower than the methane saturation, the dissolved methane gradient would be ~ 0.61 mM/m at site Pzm4W and 20% higher at site Pzm5 (0.75 mM/m; Figure 7; Supplement – Figure S14).

The presence of occluded free gas bubbles and dissolved gas migrating vertically via diffusion within the western Vestnesa Ridge segment could explain the stiffness degradation. The slow nucleation and relatively slow vertical migration of these gas bubbles by diffusion with respect to the high frequency of currents, tides and temperature change cycles will subject the gassy sediments to cyclic loading that may degrade its structure and stiffness [e.g., Katsman et al., 2013;

Barry et al., 2010]. The exact evolution of gas bubbles within the surficial sediment cannot be resolved with the data we report here (e.g., the stiffness damage by bubbles is not evident from the texture of the sediment cores in the XRF images; Figure 2). However, experimental and theoretical studies on bubble growth in fine-grained sediment show that the gas pressure, the grain size and the connectivity between micro-structures of the hosting sediment determine the way gas is transported towards the surface. For clayey material, gas can only migrate through fractures and discontinuities [Jain and Juanes, 2009b; Katsman et al., 2013]. Small, poorly interconnected pore throats will however promote internal gas bubble growth, coalescence and eventually occlusion inside the sediment, preventing gas flux from the seabed and favoring internal sediment swelling [Johnson et al., 2019].

We envision that enhanced swelling and internal bubble growth is dominant towards site 5 (the westernmost site). Pzm5 pore pressure data (pressure pulses in Figure 3) suggest that the shallowest sediment (< 5.49 mbsf) tends to trap occluded free gas bubbles and respond the most to tidal cycles [Sultan et al., 2020]. During less than 5 days of data recording, the shallow sediments at the location of Pzm5 were submitted to 11 cycles of gas expansion/exsolution/compression. This long-term gas expansion/compression cycles have likely affected its stiffness (Figure 3; Supplement – Figure S15). The formation of hydrate lenses episodically during gas expansion and exsolution cannot be excluded since the sediment interval is within the GHSZ. In this case, the coupling between free-gas expansion/exsolution and hydrate formation/dissolution would be the factor at the origin of the degradation of the sediment stiffness.

The geophysical data supports the notion of gas in the sediment. The interval that is seemingly less stiff (upper 6–7 m) is particularly well defined for the westernmost site 5 where it correlates with distinct transparent facies (i.e., the acoustic energy recorded appears attenuated) in the chirp data (Figure 6c). A transparent seismic facies and lack of strong amplitude reflections indicate more absorption of acoustic waves in the higher frequency spectrum and less acoustic impedance contrasts. Such effect on the amount of energy absorbance can be caused by the lack of sediment structure but also due to the presence of low-density (e.g., gas rich) fluids in the sediment [e.g., Anderson and Bryant, 1990; Ruppel et al., 2005].

Assuming that the westward decrease in stiffness is associated with a westward increase in the amount of gas diffused towards the surficial sediments, the question that arises is what geological mechanisms explain such a spatial variation in sub-seabed gas transport along the c. 60 km long sedimentary ridge. We address this question in the next section by discussing the observations from piezometer stations in relation to cross-disciplinary data available from the region.

5.4 Implications for understanding deformation processes, gas hydrate dynamics and seepage evolution at deep ocean basins

When placed into the geological context of the eastern Fram Strait, the analyses and interpretation of in-situ pressure and temperature data advance the discussion of the effect of glacial dynamics and tectonic forcing on the evolution of gas hydrates and seepage systems (Figure 7).

Seismic characterization and basin modeling show: 1) that seafloor pockmarks are associated with faults and fracture-controlled gas leakage from the free gas zone beneath the BSR which receives gas input from thermogenic reservoirs along the entire Vestnesa Ridge [Plaza-Faverola et al., 2017;

Daszinnies et al., 2021]; and 2) that there are spatial changes in the azimuths of faults and sizes of associated seabed pockmarks [Plaza-Faverola et al., 2015]. We therefore deliberate on the potential connection between the inferred changes in sediment stiffness, gas transport modes and the properties of faults.

The restricted distribution of acoustic flares in the east [Bünz et al., 2012; Hustoft, 2009; Plaza-Faverola et al., 2017] and the presence of wide spread methane-related pockmarks without acoustic flares in parts of the system [e.g., Consolaro et al., 2015; Vogt et al., 1994] forms the basis for arguing that the mode of gas transfer to the seafloor has experienced changes (diffusive vs. advective) in time and space. Fault-controlled gas advection was a widespread dominant mechanism along the entire sedimentary ridge but ceased towards the western Vestnesa Ridge segment shortly after the LGM (i.e., the latest methane emission events documented here date to 14–8 ky BP; Consolaro et al., 2015). Since then, gas transfer to the sub-surface occurs predominantly via diffusion. Both, diffusion and free gas advection, are processes still active at the eastern segment (Figure 7).

We argue that the response of sub-seabed faults and fractures to a dynamic stress regime determined by the simultaneous effect of glacial processes (tectonic and sedimentary) and oblique mid-ocean ridge spreading is likely the cause of the inferred spatiotemporal changes. On one hand, glacial isostatic rebound has exerted a temporal control on gas advection by regulating the opening and closing of fractures at the base of the GHSZ via slight changes in effective stresses [e.g., Grauls and Baleix, 1994]. On the other hand, spatial changes in the tectonostratigraphic stress regime have preconditioned the crust and the critically overpressured gas hydrate system [Ramachandran et al., 2022] to fracture (or not) under evolving glacial stresses.

In such a shallow sedimentary setting, the instantaneous pressure needed to shut leaking tensile fractures may closely match the fracture re-opening pressure when considering multiple cycles of leakage [e.g., Sano et al., 2005; Jain and Juanes. 2019; Noël et al., 2019; Sibson 1994; Grauls and Baleix, 1994]. Therefore, a small change in minimum horizontal stresses can make the shift between closing and re-opening pressures. Glacial stress models for the Fram Strait show that during the LGM glacial stresses at the peripheral forebulge were tensile (i.e., minimum horizontal stress c. -10 MPa; Vachon et al., [2022]). We infer that tensile glacio-tectonic stresses during the beginning of the deglaciation were favorable for reactivating near vertical-shallow faults [Steffen et al., 2014] and promoting gas advection towards the GHSZ. A shift towards negative effective stresses at the critically pressured free gas zone beneath the GHSZ would provide the condition for tensile fracturing and associated gas advection along the entire ridge. However, since the LGM, glacial stresses have been evolving into slightly less tensile to positive (i.e., minimum horizontal stress c. -6 MPa; Vachon et al., [2022]). At a critical time, glacial stresses were no longer suitable to trigger and maintain gas advection through tensile fractures in areas under larger background principal stresses [e.g., a strike-slip stress regime is inferred westward; Plaza-Faverola and Keiding, 2019] where larger pore pressures would have been required to overcome the hydro-fracturing criteria [e.g., Sibson, 1994; Sano et al., 2005; Daszinnies et al., 2021]. At present day, the glacial stress regime is presumably less suitable to trigger widespread fault reactivation and tensile fracturing but just suitable for altering favorably oriented faults [e.g., Steffen et al., 2014] in the part of the system that is under a tensile tectonic stress regime (Figure 7).

This hydromechanical model reconciles petrophysical, geophysical and geological observations from this gas hydrate and seepage system (Figure 7) and provides a possible explanation for spatiotemporal changes in gas transport modes through the GHSZ (i.e., dominance of diffusive gas flow over fracture driven or capillary invasion flow at present day in parts of the margin) and associated sediment deformation influenced by the regional stress regime. The model also provides an explanation for a correlation between paleo methane seepage events and glacial cycles documented by several authors based on sedimentary proxies [e.g., Himmler et la., 2019; Schneider et al., 2018; Dessandier et la., 2021; Consolaro et al., 2015]

Contrary to what is widely assumed (i.e., that sub-seabed deformation and fracture criteria are exclusively controlled by vertical stress) cross-disciplinary observations from this Arctic margin together with in-situ monitoring of sub-seabed pressures and temperatures (this study) provide evidence for an indirect control of the regional stress regime (and associated horizontal forcing) on seepage evolution across rifted margins. Although the data presented here are site specific, similar seemingly inactive seafloor seepage systems associated with small scale shear structures can be observed at the Hikurangi margin in a convergent setting [Plaza-Faverola et al., 2014], suggesting that localized temporal variations in horizontal forcing is an important factor controlling the spatiotemporal evolution of seepage at all type of continental/oceanic margins.

The hydromechanical parameters and relationships documented for this Arctic setting, should contribute to constrain numerical simulations of deformation processes and sediment instabilities in open ocean environments where the role of gas hydrate and associated gas reservoirs on slope stability and sliding is consistently inferred and remains highly intriguing [Elger et al., 2018; Vanneste et al., 2014].

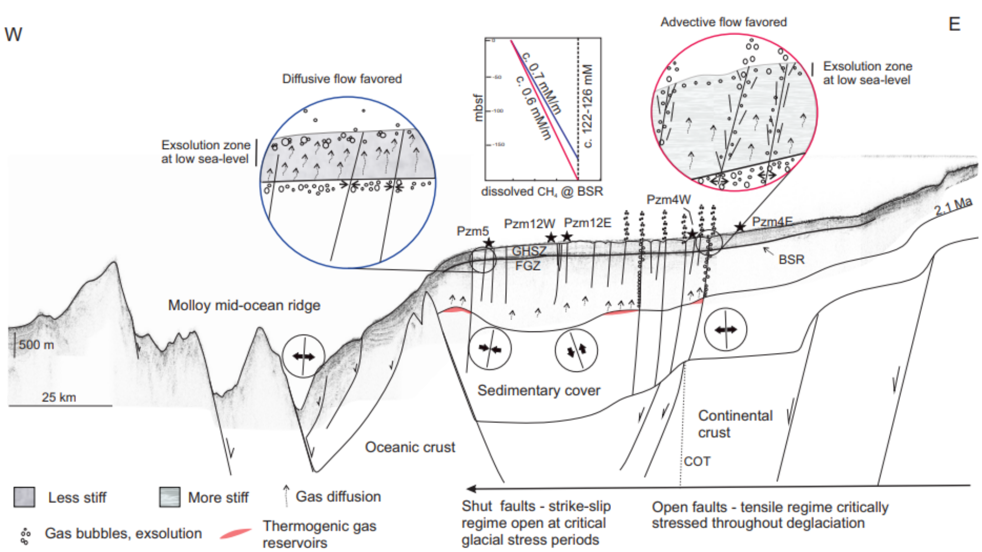

Figure 7: Conceptual model illustrating the interconnection between regional stresses, fluid flow dynamics and sub-seabed sedimentary deformation across the eastern Fram Strait. The insets illustrate the concept of enhanced diffusion/exsolution and sediment damage in the western compared to the advective dominated eastern system. Dissolved-methane gradient sketches for sites Pzm4W and Pzm5 illustrate that higher dissolved methane concentrations are expected at Pzm5 in comparison to Pzm4W because of the difference in BSR depths. The circles with the arrows illustrate the envisioned spatial variation in stress regime along the margin. GHSZ=gas hydrate stability zone; FGZ=Free gas zone; BSR=bottom simulating reflection; KR=Knipovich Ridge; MR=Molloy Ridge;

COT=Continental-Oceanic transition; Pzm stands for Piezometer and indicates the location of the piezometer sites along the E-W transect**.**

6. Conclusions

The integration of piezometer data, with geotechnical and stratigraphic analyses from sediment cores along the Vestnesa Ridge in the eastern Fram Strait, shows that there is a c. 6 m thick sediment interval beneath the seabed that is characterized by low stiffness and poor undrained cohesion. The alteration of the sediment stiffness increases westward, from the continental slope towards the mid-ocean ridge, without a distinct correlation with lithological, chronostratigraphic or consolidation state changes. We suggest this degradation of stiffness is linked to the form of gas transport and sub-surface gas exsolution in response to sea-level fluctuations. The effect of gas hydrate dissolution on the documented stiffness is a mechanism that cannot be ruled out.

Overall, the background pressure regime within the upper 10 m along the entire sedimentary ridge is at hydrostatic equilibrium. However, localized excess pore pressures exist at given structural and sedimentological conditions.

When these observations are placed into the geological context of the region, it can be inferred that:

- The amount of gas that reaches the upper few meters in the sedimentary column via diffusion increases westward, as the depth of the BSR decreases due to higher temperatures from the mid-ocean ridge.
- A few meters thick sediment interval with low stiffness and increased gas exsolution exists, that is highly sensitive to the effect of sea-level changes and cyclic sediment loading. These processes work as a pump on gassy sediments and damages the sediment structure, favoring internal gas bubble expansion/contraction and preventing methane flux into the water column.
- The fluid flow regime from the base of the gas hydrate stability zone has evolved from being dominantly advective in the past, along the entire sedimentary ridge, to be dominated by gas diffusion toward the western segment. Such change in the fluid flow regime is associated with fault responses to a dynamic stress regime. The gas hydrate system is critically pressured. A tensile background tectonic stress regime has pre-conditioned the system for fault reactivation, tensile fracturing and gas advection induced by stresses from glacial isostacy through the deglaciation periods. The present-day glacial stress regime is no longer suitable to sustain gas advection in a zone where oblique mid-ocean ridge spreading results in a more strike-slip stress regime.

As far as we are aware of, this is the first attempt to monitor the pore pressure regime across a continental slope and continental rise transect, in particular at an Arctic margin where gas hydrates, seafloor seepage and sub-seabed deformation are highly influenced by sedimentary, oceanographic and glacio-tectonic processes. The use of a multidisciplinary approach at this Arctic setting provides valuable insights into the coupling between fluid flow, near surface sedimentary deformation and regional forcing at oceanic and continental margins. The study is the first of its kind and will help constraining numerical simulations as well as improving our understanding of pre-conditioning criteria for offshore sediment instabilities.

Acknowledgments

This study is part of the SEAMSTRESS project. It is supported by starting grants from the Tromsø Research Foundation (TFS) and the Research Council of Norway (project # 287865). It is also supported by the Center for Arctic gas hydrates, environment and climate (CAGE). MME is supported by the TFS funded ARCLIM project and NeA contribution was supported by both ARCLIM and SEAMSTRESS. We are highly grateful to the ship and scientific crew on R/V Kronprins Haakon for support with deployment of piezometer and calypso core instrumentation. Special thanks to Michael Roudaut, Pierre Guyavarch and Anthony Ferrant for making possible successful collections of piezometer data over two research expeditions to the area. CRS oedometer and index tests were conducted at the Norwegian Geotechnical Institute (NGI) following their sampling protocol, in the framework of a collaboration within SEAMSTRESS. Grain size analyses and core description for site C-5 was conducted by Nessim Douss former PhD student at the University of Trieste (IT), supported by the Italian IRIDYA project (PRA-2021-0012). We are grateful to Dr. Morelia Urlaub, an anonymous reviewer, and associate Editor Brandon Dugan, for thorough revisions that helped improving the manuscript significantly. The data is deposited in DataverseNO, UiT's open research data base (https://doi.org/10.18710/GUX2O8).

References

Alexandropoulou, N., M. Winsborrow, K. Andreassen, A. Plaza-Faverola, P.-A. Dessandier, R. Mattingsdal, N. Baeten, and J. Knies (2021), A Continuous Seismostratigraphic Framework for the Western Svalbard-Barents Sea Margin Over the Last 2.7 Ma: Implications for the Late Cenozoic Glacial History of the Svalbard-Barents Sea Ice Sheet, *Frontiers in Earth Science*, *9*, 656732, https://doi.org/10.3389/feart.2021.656732

Anderson, A. L., and W. R. Bryant (1990), Gassy sediment occurrence and properties: Northern Gulf of Mexico, *Geo-Marine Letters*, *10*(4), 209-220. https://doi.org/10.1007/BF02431067

Astm, D. (2004), 2435, *Standard Test Methods for One Dimensional Consolidation Properties of Soils using Incremental Loading*.

Astm, International (2006), Standard test method for one-dimensional consolidation properties of saturated cohesive soils using controlled-strain loading (Standard D4186–06), in Annual Book of ASTM Standards, vol. 04.08, Soil and Rock (I), pp. 1–15, West Conshohocken, Pa

Barry, M. A., B. P. Boudreau, B. D. Johnson, and A. H. Reed (2010), First-order description of the mechanical fracture behavior of fine-grained surficial marine sediments during gas bubble growth, *Journal of Geophysical Research: Earth Surface*, *115*(F4), https://doi.org/10.1029/2010JF001833

Blouin, A., N. Sultan, J.-P. Callot, and P. Imbert (2019), Sediment damage caused by gas exsolution: A key mechanism for mud volcano formation, *Engineering Geology*, *263*, 105313; https://doi.org/10.1016/j.enggeo.2019.105313

Bolton, A., and A. Maltman (1998), Fluid-flow pathways in actively deforming sediments: the role of pore fluid pressures and volume change, *Marine and Petroleum Geology*, *15*(4), 281-297; https://doi.org/10.1016/S0264-8172(98)00025-7

Boudreau, B. P., C. Algar, B. D. Johnson, I. Croudace, A. Reed, Y. Furukawa, K. M. Dorgan, P. A. Jumars, A. S. Grader, and B. S. Gardiner (2005), Bubble growth and rise in soft sediments, *Geology*, *33*(6), 517-520, doi:10.1130/g21259.1.

Boudreau, B. R. (2012), The physics of bubbles in surficial, soft, cohesive sediments, *Marine and Petroleum Geology*, *38*(1), 1-18, doi:10.1016/j.marpetgeo.2012.07.002.

Burns, S. E., and P. W. Mayne (1998), Monotonic and dilatory pore-pressure decay during piezocone tests in clay, *Canadian Geotechnical Journal*, *35*(6), 1063-1073; https://doi.org/10.1139/t98-06

Burns, S. E., and P. W. Mayne (2002), Analytical cavity expansion-critical state model for piezocone dissipation in fine-grained soils, *Soils and Foundations*, *42*(2), 131-137; https://doi.org/10.3208/sandf.42.2_131

Bünz, S., S. Polyanov, S. Vadakkepuliyambatta, C. Consolaro, and J. Mienert (2012), Active gas venting through hydrate-bearing sediments on the Vestnesa Ridge, offshore W-Svalbard, *Marine geology*; https://doi.org/10.1016/j.margeo.2012.09.012

Caricchi, C., R. G. Lucchi, L. Sagnotti, P. Macrì, A. Di Roberto, P. Del Carlo, K. Husum, J. S. Laberg, and C. Morigi (2019), A high-resolution geomagnetic relative paleointensity record from the Arctic Ocean deep-water gateway deposits during the last 60 kyr, *Geochemistry, Geophysics, Geosystems*, *20*(5), 2355-2377.

Chauhan, T., T. L. Rasmussen, and R. Noormets (2016), Palaeoceanography of the Barents Sea continental margin, north of Nordaustlandet, Svalbard, during the last 74 ka, Boreas, 45(1), 76-99.

Christian, H., D. Heffler, and E. Davis (1993), Lancelot—an in situ piezometer for soft marine sediments, *Deep Sea Research Part I: Oceanographic Research Papers*, *40*(7), 1509-1520.

Clennell, M. B., A. Judd, and M. Hovland (2000), Movement and accumulation of methane in marine sediments: Relation to gas hydrate systems, in *Natural gas hydrate*, edited, pp. 105-122, Springer.

Consolaro, C., T. Rasmussen, G. Panieri, J. Mienert, S. Bünz, and K. Sztybor (2015), Carbon isotope (δ 13 C) excursions suggest times of major methane release during the last 14 kyr in Fram Strait, the deep-water gateway to the Arctic, *Climate of the Past*, *11*(4), 669-685.

Crane, K., E. Sundvor, J. P. Foucher, M. Hobart, A. M. Myhre, and S. LeDouaran (1988), Thermal evolution of the western Svalbard margin, *Marine geophysical researches*, *9*(2), 165-194.

Daszinnies, M., A. Plaza-Faverola, Ø. Sylta, S. Bünz, R. Mattingsdal, A. Tømmerås, and J. Knies (2021), The Plio-Pleistocene seepage history off western Svalbard inferred from 3D petroleum systems modelling, *Marine and Petroleum Geology*, *128*, 105023.

Dessandier, P.-A., J. Knies, A. Plaza-Faverola, C. Labrousse, M. Renoult, and G. Panieri (2021), Ice-sheet melt drove methane emissions in the Arctic during the last two interglacials, Geology, 49(7), 799-803

Dugan, B., and T. Sheahan (2012), Offshore sediment overpressures of passive margins: Mechanisms, measurement, and models, *Reviews of Geophysics*, *50*(3).

Eiken, O., and K. Hinz (1993), Contourites in the Fram Strait, *Sedimentary Geology*, *82*(1), 15-32.

Elger, J., C. Berndt, L. Rüpke, S. Krastel, F. Gross, and W. H. Geissler (2018), Submarine slope failures due to pipe structure formation, *Nature Communications*, *9*(1), 1-6.

Elverhøi, A., J. I. Svendsen, A. Solheim, E. S. Andersen, J. Milliman, J. Mangerud, and R. L. Hooke (1995), Late Quaternary sediment yield from the high Arctic Svalbard area, *The Journal of Geology*, *103*(1), 1-17.

Engen, Ø., J. I. Faleide, and T. K. Dyreng (2008), Opening of the Fram Strait gateway: A review of plate tectonic constraints, *Tectonophysics*, *450*(1), 51-69.

Fleischer, P., T. Orsi, M. Richardson, and A. Anderson (2001), Distribution of free gas in marine sediments: a global overview, *Geo-Marine Letters*, *21*(2), 103-122.

Goswami, B. K., Weitemeyer, K. A., Minshull, T. A., Sinha, M. C., Westbrook, G. K., Chabert, A., Henstock, T. J., and Ker, S., 2015, A joint electromagnetic and seismic study of an active pockmark within the hydrate stability field at the Vestnesa Ridge, West Svalbard margin: Journal of Geophysical Research: Solid Earth, v. 120, no. 10, p. 6797-6822.

Grauls, D., and J. Baleix (1994), Role of overpressures and in situ stresses in fault-controlled hydrocarbon migration: A case study, Marine and Petroleum Geology, 11(6), 734-742.

Gupta, S., C. Schmidt, C. Böttner, L. H. Rüpke, and E. L. Hartz (2021), Spontaneously exsolved free gas during major storms as a driver for pockmark formation, *Geochemistry, Geophysics, Geosystems*.

Hight, D. W., and S. Leroueil (2003), Characterisation of soils for engineering purposes, *Characterisation and engineering properties of natural soils*, *1*, 255-360.

Himmler, T., D. Sahy, T. Martma, G. Bohrmann, A. Plaza-Faverola, S. Bünz, D. J. Condon, J. Knies, and A. Lepland (2019), A 160,000-year-old history of tectonically controlled methane seepage in the Arctic, *Science advances*, *5*(8), eaaw1450.

Hong, W.-L., T. Pape, C. Schmidt, H. Yao, K. Wallmann, A. Plaza-Faverola, J. Rae, A. Lepland, S. Bünz, and G. Bohrmann (2021), Interactions between deep formation fluid and gas hydrate dynamics inferred from pore fluid geochemistry at active pockmarks of the Vestnesa Ridge, west Svalbard margin, *Marine and Petroleum Geology*, *127*, 104957.

Hong, Y., L. Wang, B. Yang, and J. Zhang (2019), Stress-dilatancy behaviour of bubbled fine-grained sediments, *Engineering Geology*, *260*, 105196.

Howe, J. A., T. M. Shimmield, R. Harland, and N. Eyles (2008), Late Quaternary contourites and glaciomarine sedimentation in the Fram Strait, *Sedimentology*, *55*(1), 179-200.

Hustoft, S., Bunz, S., Mienert, J., Chand, S. (2009), Gas hydrate reservoir and active methane-venting province in sediments on < 20 Ma young oceanic crust in the Fram Strait, offshore NW-Svalbard, *Earth and Planetary Science Letters*, *284*(1-2), 12-24, doi:10.1016/j.epsl.2009.03.038.

Jain, A., and R. Juanes (2009), Preferential mode of gas invasion in sediments: Grain-scale mechanistic model of coupled multiphase fluid flow and sediment mechanics, *Journal of Geophysical Research: Solid Earth*, *114*(B8).

Jessen, S. P., and T. L. Rasmussen (2015), Sortable silt cycles in Svalbard slope sediments 74–0 ka, Journal of Quaternary Science, 30(8), 743-753, https://doi.org/10.1002/jqs.2807.

Jessen, S. P., and T. L. Rasmussen (2019), Ice-rafting patterns on the western Svalbard slope 74–0 ka: interplay between ice-sheet activity, climate and ocean circulation, *Boreas*, *48*(1), 236-256.

Jessen, S. P., T. L. Rasmussen, T. Nielsen, and A. Solheim (2010), A new Late Weichselian and Holocene marine chronology for the western Svalbard slope 30,000–0 cal years BP, *Quaternary Science Reviews*, *29*(9-10), 1301-1312.

Johnson, B. D., B. P. Boudreau, B. S. Gardiner, and R. Maass (2002), Mechanical response of sediments to bubble growth, *Marine Geology*, *187*(3-4), 347-363.

Johnson, M., J. Peakall, M. Fairweather, M. Barnes, S. Davison, X. Jia, M. A. Clare, D. Harbottle, and T. N. Hunter (2019), Sediment microstructure and the establishment of gas migration pathways during bubble growth, *Environmental Science & Technology*, *53*(21), 12882-12892.

Katsman, R., I. Ostrovsky, and Y. Makovsky (2013), Methane bubble growth in fine-grained muddy aquatic sediment: insight from modeling, *Earth and Planetary Science Letters*, *377*, 336-346.

Knies, J., and S. Vadakkepuliyambatta (2019), CAGE19-3 Cruise Report: Calypso giant piston coring in the Atlantic-Arctic gateway–Investigation of continental margin development and effect of tectonic stress on methane release, CAGE–Centre for Arctic Gas Hydrate, Environment and Climate Report Series, 7.

Knies, J., M. Daszinnies, A. Plaza-Faverola, S. Chand, Ø. Sylta, S. Bünz, J. E. Johnson, R. Mattingsdal, and J. Mienert (2018), Modelling persistent methane seepage offshore western Svalbard since early Pleistocene, *Marine and Petroleum Geology*, *91*, 800-811.

Knies, J., R. Mattingsdal, K. Fabian, K. Grøsfjeld, S. Baranwal, K. Husum, S. De Schepper, C. Vogt, N. Andersen, and J. Matthiessen (2014), Effect of early Pliocene uplift on late Pliocene cooling in the Arctic–Atlantic gateway, *Earth and Planetary Science Letters*, *387*, 132-144.

Lei, L., and J. C. Santamarina (2019), Physical properties of fine-grained sediments with segregated hydrate lenses, Marine and Petroleum Geology, 109, 899-911.

Liu, X., and P. B. Flemings (2006), Passing gas through the hydrate stability zone at southern Hydrate Ridge, offshore Oregon, *Earth and Planetary Science Letters*, *241*(1-2), 211-226.

Locat, J., and H. J. Lee (2002), Submarine landslides: advances and challenges, *Canadian Geotechnical Journal*, *39*(1), 193-212.

Lucchi, R., A. Camerlenghi, M. Rebesco, E. Colmenero-Hidalgo, F. Sierro, L. Sagnotti, R. Urgeles, R. Melis, C. Morigi, and M.-A. Bárcena (2013), Postglacial sedimentary processes on the Storfjorden and Kveithola trough mouth fans: Significance of extreme glacimarine sedimentation, *Global and planetary change*, *111*, 309-326.

Lucchi, R. G., L. Sagnotti, A. Camerlenghi, P. Macrì, M. Rebesco, M. T. Pedrosa, and G. Giorgetti (2015), Marine sedimentary record of Meltwater Pulse 1a along the NW Barents Sea continental margin, *arktos*, *1*(1), 1-14.

Lunne, T, Berre, T, Stranvik, S, Andersen, KH, & Tjelta, TI (2001). Deepwater sample disturbance due to stress relief. Proceedings of the OTRC 2001 international conference, Houston, TX, pp. 64–85.Mattingsdal, R., J. Knies, K. Andreassen, K. Fabian, K. Husum, K. Grøsfjeld, and S. De Schepper (2014), A new 6 Myr stratigraphic framework for the Atlantic–Arctic Gateway, *Quaternary Science Reviews*, *92*, 170-178.

Nielsen, T., T. Rasmussen, S. Ceramicola, and A. Kuijpers (2007), Quaternary sedimentation, margin architecture and ocean circulation variability around the Faroe Islands, North Atlantic, *Quaternary Science Reviews*, *26*(7-8), 1016-1036.

Noël, C., F. X. Passelègue, C. Giorgetti, and M. Violay (2019), Fault reactivation during fluid pressure oscillations: Transition from stable to unstable slip, Journal of Geophysical Research: Solid Earth, 124(11), 10940-10953

Panieri, G., S. Bünz, D. J. Fornari, J. Escartin, P. Serov, P. Jansson, M. E. Torres, J. E. Johnson, W. Hong, and S. Sauer (2017), An integrated view of the methane system in the pockmarks at Vestnesa Ridge, 79 N, *Marine Geology*, *390*, 282-300.

Pape, T., S. Buenz, W. L. Hong, M. E. Torres, M. Riedel, G. Panieri, A. Lepland, C. W. Hsu, P. Wintersteller, and K. Wallmann (2020), Origin and transformation of light hydrocarbons ascending at an active pockmark on Vestnesa Ridge, Arctic Ocean, *Journal of Geophysical Research: Solid Earth*, *125*(1), e2018JB016679.

Petersen, C. J., S. Bünz, S. Hustoft, J. Mienert, and D. Klaeschen (2010), High-resolution P-Cable 3D seismic imaging of gas chimney structures in gas hydrated sediments of an Arctic sediment drift, *Marine and Petroleum Geology*, *doi: 10.1016/j.marpetgeo.2010.06.006*, 1-14, doi:DOI: 10.1016/j.marpetgeo.2010.06.006.

Plaza-Faverola, A., and M. Keiding (2019), Correlation between tectonic stress regimes and methane seepage on the western Svalbard margin, *Solid Earth*, *10*(1), 79-94.

Plaza-Faverola, A., S. Vadakkepuliyambatta, W. L. Hong, J. Mienert, S. Bunz, S. Chand, and J. Greinert (2017), Bottom-simulating reflector dynamics at Arctic thermogenic gas provinces: An example from Vestnesa Ridge, offshore west Svalbard, *Journal of Geophysical Research-Solid Earth*, *122*(6), 4089-4105, doi:10.1002/2016jb013761.

Plaza-Faverola, A., S. Bünz, J. E. Johnson, S. Chand, J. Knies, J. Mienert, and P. Franek (2015), Role of tectonic stress in seepage evolution along the gas hydrate-charged Vestnesa Ridge, Fram Strait, *Geophysical Research Letters*, *42*(3), 733-742.

Plaza-Faverola, A., I. Pecher, G. Crutchley, P. M. Barnes, S. Bünz, T. Golding, D. Klaeschen, C. Papenberg, and J. Bialas (2014), Submarine gas seepage in a mixed contractional and shear deformation regime: Cases from the Hikurangi oblique-subduction margin, *Geochemistry, Geophysics, Geosystems*, *15*(2), 416-433.

Plaza-Faverola, A. (2020), CAGE20-6 Cruise Report: Pore-fluid pressure and heat flow surveys along the Vestnesa Ridge, west-Svalbard continental margin, CAGE–Centre for Arctic Gas Hydrate, Environment and Climate Report Series, 8.Puzrin, A. M., J. Tront, A. Schmid, and J. B. Hughes (2011), Engineered use of microbial gas production to decrease primary consolidation settlement in clayey soils, *Géotechnique*, *61*(9), 785-794.

Ramachandran, H., A. Plaza-Faverola, and H. Daigle (2022), Impact of Gas Saturation and Gas Column Height at the Base of the Gas Hydrate Stability Zone on Fracturing and Seepage at Vestnesa Ridge, West-Svalbard Margin, *Energies*, *15*(9), 3156.

Ruppel, C., G. Dickens, D. Castellini, W. Gilhooly, and D. Lizarralde (2005), Heat and salt inhibition of gas hydrate formation in the northern Gulf of Mexico, *Geophysical Research Letters*, *32*(4).

Sano, O., H. Ito, A. Hirata, and Y. Mizuta (2005), Review of methods of measuring stress and its variations, Bull. Earthq. Res. Inst. Univ. Tokyo, 80, 87-103.

Schneider, A., G. Panieri, A. Lepland, C. Consolaro, A. Crémière, M. Forwick, J. E. Johnson, A. Plaza-Faverola, S. Sauer, and J. Knies (2018), Methane seepage at Vestnesa Ridge (NW svalbard) since the last glacial maximum, *Quaternary Science Reviews*, *193*, 98-117.

Sibson, R. H. (1994), Crustal stress, faulting and fluid flow, *Geological Society, London, Special Publications*, *78*(1), 69-84.

Sills, G. C., S. J. Wheeler, S. D. Thomas, and T. N. Gardner (1991), BEHAVIOR OF OFFSHORE SOILS CONTAINING GAS-BUBBLES, *Geotechnique*, *41*(2), 227-241.

Singhroha, S., S. Bünz, A. Plaza-Faverola, and S. Chand (2016), Gas hydrate and free gas detection using seismic quality factor estimates from high-resolution P-cable 3D seismic data, *Interpretation*, *4*(1), SA39-SA54.

Singhroha, S., S. Bünz, A. Plaza-Faverola, and S. Chand (2020), Detection of gas hydrates in faults using azimuthal seismic velocity analysis, Vestnesa Ridge, W-Svalbard Margin, *Journal of Geophysical Research: Solid Earth*, *125*(2), e2019JB017949.

Singhroha, S., S. Chand, and S. Bünz (2019), Constraints on gas hydrate distribution and morphology in Vestnesa Ridge, western Svalbard margin, using multicomponent ocean-bottom seismic data, *Journal of Geophysical Research: Solid Earth*, *124*(5), 4343-4364.

Skempton, A. (1964), Long-term stability of clay slopes, *Geotechnique*, *14*(2), 77-102.

Skempton, A. W. (1957), Discussion: Further data on the c/p ratio in normally consolidated clays, *proceedings of the institution of civil engineers*, *7*, 305-307.

Smith, A. J., J. Mienert, S. Bünz, and J. Greinert (2014), Thermogenic methane injection via bubble transport into the upper Arctic Ocean from the hydrate-charged Vestnesa Ridge, Svalbard, *Geochemistry, Geophysics, Geosystems*.

Sobkowicz, J. C., and N. R. Morgenstern (1984), THE UNDRAINED EQUILIBRIUM BEHAVIOR OF GASSY SEDIMENTS, *Canadian Geotechnical Journal*, *21*(3), 439-448.

Spivey, J. P., W. D. McCain, and R. North (2004), Estimating density, formation volume factor, compressibility, methane solubility, and viscosity for oilfield brines at temperatures from 0 to 275 C, pressures to 200 MPa, and salinities to 5.7 mole/kg, Journal of Canadian Petroleum Technology, 43(07), https://doi.org/10.2118/04-07-05

Steffen, R., H. Steffen, P. Wu, and D. W. Eaton (2014), Stress and fault parameters affecting fault slip magnitude and activation time during a glacial cycle, *Tectonics*, *33*(7), 1461-1476.

Sultan, N. (2007), Comment on "Excess pore pressure resulting from methane hydrate dissociation in marine sediments: A theoretical approach" by Wenyue Xu and Leonid N. Germanovich, *Journal of Geophysical Research-Solid Earth*, *112*(B2), doi:B0210310.1029/2006jb004527.

Sultan, N., V. De Gennaro, and A. Puech (2012), Mechanical behaviour of gas-charged marine plastic sediments, *Geotechnique*, *62*(9), 751-766, doi:10.1680/geot.12.OG.002.

Sultan, N., and S. Lafuerza (2013), In situ equilibrium pore-water pressures derived from partial piezoprobe dissipation tests in marine sediments, *Canadian Geotechnical Journal*, *50*(12), 1294-1305 https://doi.org/10.1139/cgj-2013-0062

Sultan, N., et al. (2010), Hydrate dissolution as a potential mechanism for pockmark formation in the Niger delta, *Journal of Geophysical Research-Solid Earth*, *115*, doi:10.1029/2010jb007453.

Sultan, N., A. Plaza-Faverola, S. Vadakkepuliyambatta, S. Buenz, and J. Knies (2020), Impact of tides and sea-level on deep-sea Arctic methane emissions, *Nature communications*, *11*(1), 1-10 https://doi.org/10.1038/s41467-020-18899-3

Sztybor, K., and T. L. Rasmussen (2017), Late glacial and deglacial palaeoceanographic changes at Vestnesa Ridge, Fram Strait: Methane seep versus non-seep environments, *Palaeogeography, Palaeoclimatology, Palaeoecology*, *476*, 77-89.

Taleb, F., S. Garziglia, and N. Sultan (2018), Hydromechanical properties of gas hydrate-bearing fine sediments from in situ testing, *Journal of Geophysical Research: Solid Earth*, *123*(11), 9615-9634.

Terzariol, M., N. Sultan, R. Apprioual, and S. Garziglia (2021), Pore habit of gas in gassy sediments, *Journal of Geophysical Research: Solid Earth*, *126*(5), e2020JB021511.

Thomas, S. D. (1987), The consolidation behaviour of gassy soil (Doctoral dissertation, University of Oxford).

Vachon, R., P. Schmidt, B. Lund, A. Plaza-Faverola, H. Patton, and A. Hubbard (2022), Glacially Induced Stress Across the Arctic From the Eemian Interglacial to the Present—Implications for Faulting and Methane Seepage, *Journal of Geophysical Research: Solid Earth*, *127*(7), e2022JB024272.

VanderBeek, B. P., and A. W. Rempel (2018), On the importance of advective versus diffusive transport in controlling the distribution of methane hydrate in heterogeneous marine sediments, *Journal of Geophysical Research: Solid Earth*, *123*(7), 5394-5411.

Vanneste, M., S. Guidard, and J. Mienert (2005), Arctic gas hydrate provinces along the western Svalbard continental margin, *Norwegian Petroleum Society Special Publications*, *12*, 271-284.

Vanneste, M., N. Sultan, S. Garziglia, C. F. Forsberg, and J.-S. L'Heureux (2014), Seafloor instabilities and sediment deformation processes: The need for integrated, multi-disciplinary investigations, *Marine Geology*, *352*, 183-214.

Velde, B. (1996), Compaction trends of clay-rich deep sea sediments, *Marine Geology*, *133*(3-4), 193-201.

Vogt, P. R., K. Crane, E. Sundvor, M. D. Max, and S. L. Pfirman (1994), Methane-generated (?) pockmarks on young, thickly sedimented oceanic crust in the Arctic: Vestnesa Ridge, Fram strait, *Geology*, *22*(3), 255-258.

Waite, W. F., et al. (2009), PHYSICAL PROPERTIES OF HYDRATE-BEARING SEDIMENTS, *Reviews of Geophysics*, *47*, doi:10.1029/2008rg000279.

Wheeler, S. J. (1988), THE UNDRAINED SHEAR-STRENGTH OF SOILS CONTAINING LARGE GAS-BUBBLES, *Geotechnique*, *38*(3), 399-413.

Yoneda, J., A. Masui, Y. Konno, Y. Jin, M. Kida, J. Katagiri, J. Nagao, and N. Tenma (2017), Pressure-core-based reservoir characterization for geomechanics: Insights from gas hydrate drilling during 2012–2013 at the eastern Nankai Trough, *Marine and Petroleum Geology*, *86*, 1-16.

Zhang, Y. X., and Z. J. Xu (2003), Kinetics of convective crystal dissolution and melting, with applications to methane hydrate dissolution and dissociation in seawater, *Earth and Planetary Science Letters*, *213*(1-2), 133-148, doi:10.1016/s0012-821x(03)00297-8.

Zhou, X., and R. Katsman (2022), Mechanical controls on methane bubble solute exchange within muddy aquatic sediments and its growth characteristics, *Journal of Structural Geology*, *161*, 104642.

Zhu, B., J. Huang, L. Wang, and Z. Ye (2021), Precise numerical study on the behaviour of gassy marine soils subjected to thermal and mechanical loadings, *Computers and Geotechnics*, *137*, 104269.

[Journal of Geophysical Research, Solid Earth]

Supporting Information for

[Spatial changes in gas transport and sediment stiffness influenced by regional stress: observations from piezometer data along Vestnesa Ridge, eastern Fram Strait]

[Andreia Plaza-Faverola[1]; Nabil Sultan[2]; Renata G. Lucchi[3]; Naima El bani Altuna[1]; Hariharan Ramachandran[1]; Sunny Singhroha[1]; Frances Cooke[1]; Sunil Vadakkepuliyambatta[4]; Mohamed M. Ezat[1]; Tine L. Rasmussen[1]]

[1-CAGE-Centre for Arctic Gas Hydrate, Environment, and Climate, Department of Geosciences, UiT-the Arctic University of Norway, Tromsø, Norway
2-Geo-Ocean, UMR6538, Ifremer, CNRS, UBO, UBS, 29280 Plouzané, France
3- National Institute of Oceanography and Applied Geophysics – OGS, Trieste, Italy
4- National Centre for Polar and Ocean Research, Ministry of Earth Sciences, Vasco-da-Gama, Goa, India]

Contents of this file

Text S1 – oedometer tests

Oedometer tests were conducted at wholearound sub-samples from 2 depth intervals along each core using a constant rate of strain (CRS) [*ASTM International*, 2006] at the labs by the Norwegian Geotechnical Institute (NGI). In addition, oedometer tests with incremental loading were performed on ten samples (Table S 1) using incremental loading according to the ASTM D-2435 method [*Astm*, 2004]. The aim is to characterize both the consolidation/compressibility characteristics and permeability. During incremental consolidation tests, the falling-head method is used to determine the permeability (or hydraulic conductivity) of the sediment samples. Sediment samples were selected from two different sites (C-05 and C-12 – Figure 1 main text) investigated during the CAGE 19-3 cruise of RV "Kronprins Haakon" [*Knies and Vadakkepuliyambatta*, 2019]. The two sites were chosen near the piezometers Pzm05 and Pzm12W deployed to characterize the in-situ thermal and hydraulic regimes.

Table S1 indicates the characteristics of the ten tests carried out on two sediment Calypso cores (C-05 and C-12). Column four in Table S1 specifies the quality of the tested samples based on the criteria in [*Lunne and Long*, 2006]. Based on MSCL P-wave and ρ-density log data, six samples were selected from site 5 (black horizontal triangles in Figure S1) and four samples from site 12 (black horizontal triangles in Figure S2). Depths at which the samples were selected correspond to the position of six sensors of the piezometer Pzm5 and four sensors of the Pzm12W (red dash lines in Figure S1 and Figure S2).

Figure S3 summarizes the experimental results of the CRS oedometer test showing the change of the void ratio as a function of the axial effective stress.

Figures S4 and S5 summarizes the experimental results of the oedometer tests (incremental loading) with the void ratio, permeability and coefficient of consolidation versus effective axial stress.

Figures S3 to S5 show the data used to determine the compressibility indexes (*Cc)*.

Text S2 – sedimentological data

Sedimentological data from calypso cores C-4, C-12 and C-5 are shown in Figures S6 to S8. Bulk density, P-Wave velocity, XRF mineral ratio logs, water content, and the visual core description, are included in addition to grain size and magnetic susceptibility presented in figure 2 in the main text.

Text S3 – piezometer data

As shown in Figure 3, most of the pore-pressure dissipation curves did not reach the equilibrium pressure (Δu_{eq}). The modified cavity expansion approach proposed by [*Sultan and Lafuerza*, 2013] aims to simulate this pore water dissipation process from partial measurements of the in-situ pore water pressure. The details on the method are described in Sultan and Lafuerza [2013] for the cylindrical and spherical cases. Hereby we include the main equations and the numerical approach used for the cylindrical expansion case where the dissipation of Δu(r,t) with time is calculated using the following consolidation equation [*Burns and Mayne*, 1998]:

$$\frac{\partial(\Delta u)}{\partial t} = \frac{C_h}{r}\frac{\partial(\Delta u)}{\partial r} + C_h\frac{\partial^2(\Delta u)}{\partial r^2} \qquad \text{(eq S1)}$$

Where r varies between r_0 the radius of the piezometer rod and r_p the radius of the sheared and plasticized zones determined using the cavity expansion theory [*Burns and Mayne*, 1998]:

$$r_p = r_0\sqrt{I_r} = r_0\sqrt{\frac{G}{Su}} \qquad \text{(eq S2)}$$

Where S_u is the undrained shear strength and G is the shear modulus.

In the approach by Sultan and Lafuerza [2013], the coefficient of consolidation C_h is considered to change linearly during the dissipation process (from C_{hi} to $(1-\beta)\ C_{hi}$) and it decreases with time according to the following equation [*Abuel-Naga and Pender*, 2012]:

$$C_h = C_{hi}\left[1 - \beta\frac{\Delta u_i - \Delta u}{\Delta u_i - \Delta u_{eq}}\right] \qquad \text{(eq S3)}$$

Where Δu is excess pore pressure and β corresponds to the Abuel-Naga and Pender [2012] “icv” dimensionless parameter. β(=icv) describes the change of the coefficient of consolidation with the consolidation stress increment. The aim of this method is to predict accurately the Δu_{eq} integrating partial dissipation tests. In order to fulfil this main goal, equations S1 to S3 were numerically solved by approximating all the derivatives by finite differences and by using an explicit numerical method. A numerical scheme similar to the one proposed by [*Kim and Lee*, 2000] was implemented (Figure 3) and solved using the fortran programming language. The calculation of the excess pore pressure evolution with time at a given sensor leads to consider numerically the change in Δu in space r (with $r_0 \leq r \leq r_p$) and time t (with $t \geq 0$). In addition, the numerical calculation requires the specification of boundary conditions at $r = r_0$ and $r = r_p$, and initial conditions at time t = 0. The limit conditions are as follow: impermeable wall at $r=r_0$ and $\Delta u=\Delta u_{eq}$ at $r=r_p$. At t=0, the pore pressure Δu_i at $r=r_0$ is measured by the piezometer and considered as an input in the calculation.

An iterative procedure is necessary to determine the more appropriate values for the unknowns of the problem (C_h, β, Ir and Δu_{eq}) by means of an optimization algorithm. This becomes a numerical problem that consists in finding a set of variables that gives the minimum error between measured and predicted pore pressure at a given sensor. The uniqueness of the solution and therefore the correctness of the prediction of the unknowns depend on the time length of the dissipation test. Sultan and Lafuerza [2013] defined the following criterion to accurately calculate the in-situ equilibrium excess pore pressures (Δu_{eq}): the second derivative of pore pressure, Δu, versus the logarithmic of time, t, must be positive $\left(\frac{\partial^2 \Delta u}{\partial ln(t)^2} > 0\right)$. They also showed that a dissipation pore-water pressure curve matches with a unique value of $\frac{C_h}{\sqrt{I_r}}$ that may correspond to infinite couples of “rigidity index - I_r” and “hydraulic diffusivity - C_h”. It becomes therefore impossible to derive I_r and C_h for unknown sediments from a dissipation pore-water pressure curve alone [*Sultan and Lafuerza*, 2013].

In this study, the cavity expansion method developed by Sultan and Lafuerza [2013] was applied for 35 dissipation curves where the $\frac{\partial^2 \Delta u}{\partial ln(t)^2}$ criteria was fulfilled (Figures S5 to S9). For 3 dissipation curves, the recording time was not long enough to perform the calculation (Figures S8 and S9). For Pzm5 (Figure S5), the upper pore pressure curves were very noisy (i.e., strong pressure fluctuations) to be analyzed. The calculation results in Figures S5 to S9 show that for an average of three calculation runs per sensor (red, blue and green curves), the dissipation solution was almost unique with very low variability in Δu_{eq} and $\frac{C_h}{\sqrt{I_r}}$ (Figure 4).

Text S4 – Methane solubility

The methane solubility at the bottom simulating reflection (BSR) depth at both sites Pzm5 and Pzm4W was calculated using the method of [*Spivey et al.*, 2004] by considering the salinity, temperature and pressure conditions at the base of the BSR. The temperature was calculated by considering a permanent thermal regime (constant thermal gradient) and the seabed temperature (Figure S14). The pressure was calculated by assuming hydrostatic conditions. For Pzm5 (depth=170 mbsf; T= -1.05°C; salinity= 34.5 g/L), the methane solubility χ is found to be equal to 123 mM while for the Pzm4W conditions (depth=200 mbsf; T= -0.95°C; salinity= 34.5 g/L) χ is equal to 126 mM (Figure S14).

Text S5 – Δu versus tide cycles

The data collected from Pzm5 provide insights into the variation of the Δu values with tide cycles. Although one would expect that the use of differential pressure sensors will eliminate the effects of tide cycles on the measured Δu, observed perturbations occurring during the low and ascendant tide cycle phases suggest that the dynamics of free gas, which increases the compressibility of the pore fluid, is affecting the pore pressure measurements (Figure S15). Red periods in Figure S15-a correspond to gas exsolution and expansion while black periods indicate gas dissolution and compression. The perturbation of Δu is expected to be proportional to the gas content [*Garziglia et al.*, 2021].

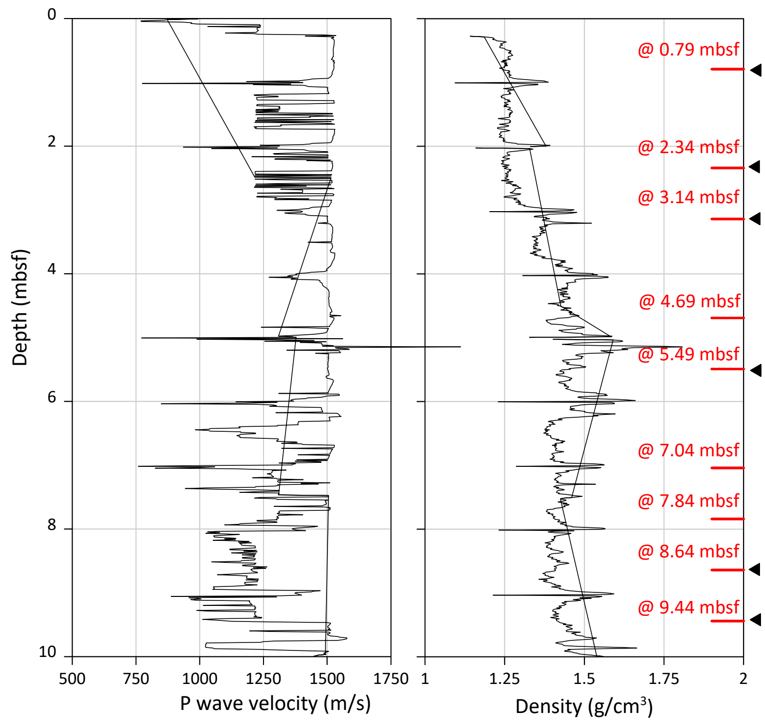

Figure S1. Core C-05. Six samples selected to carry out oedometer tests based on core P wave and ρ-density log data.

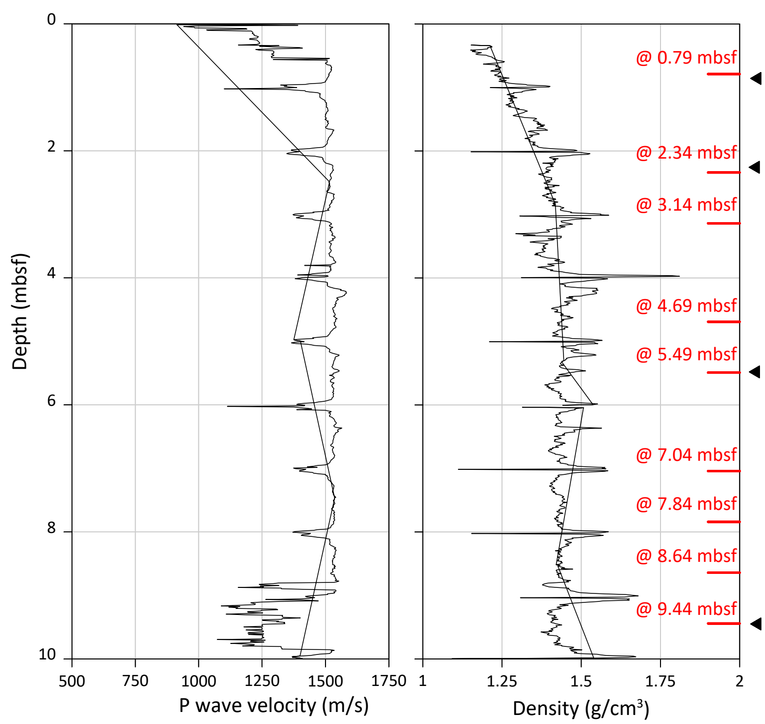

Figure S2. Core C-12. Six samples selected to carry out oedometer tests based on core P wave and ρ-density log data.

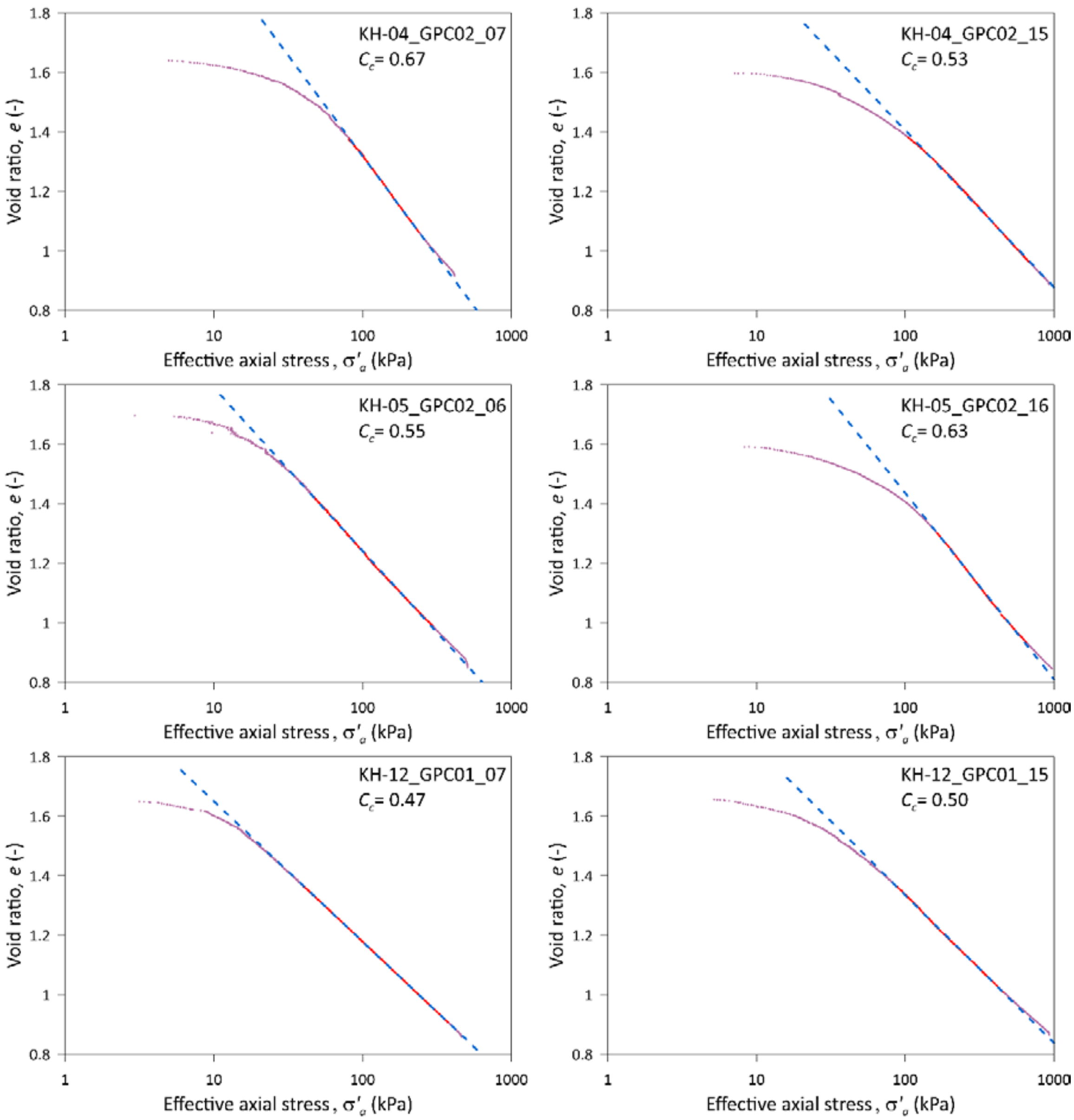

Figure S3. Summary of one dimensional oedometer tests (CRS).

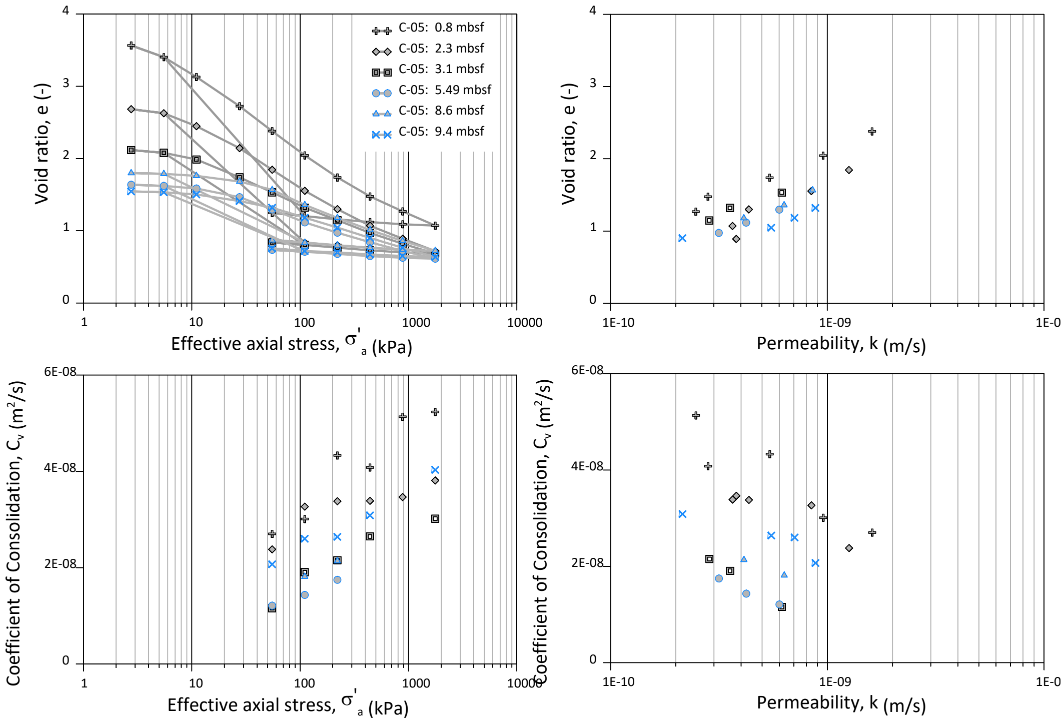

Figure S4. Core C-05. Summary of one dimensional oedometer tests (incremental loading).

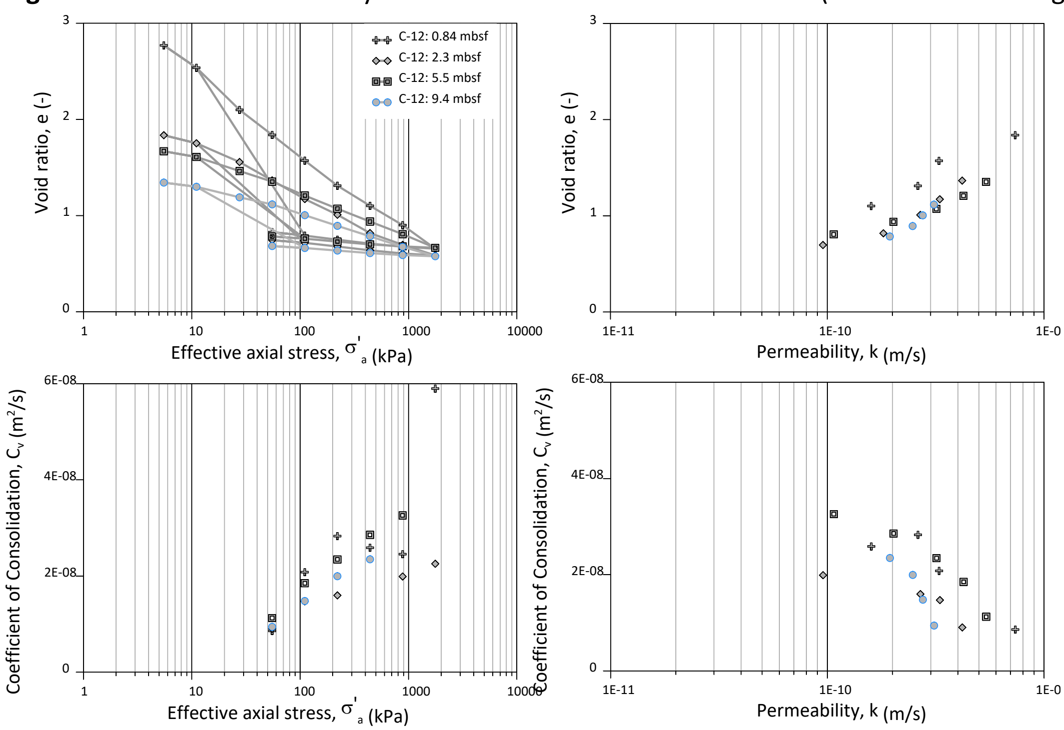

Figure S5. Core C-12. Summary of one dimensional oedometer tests (incremental loading).

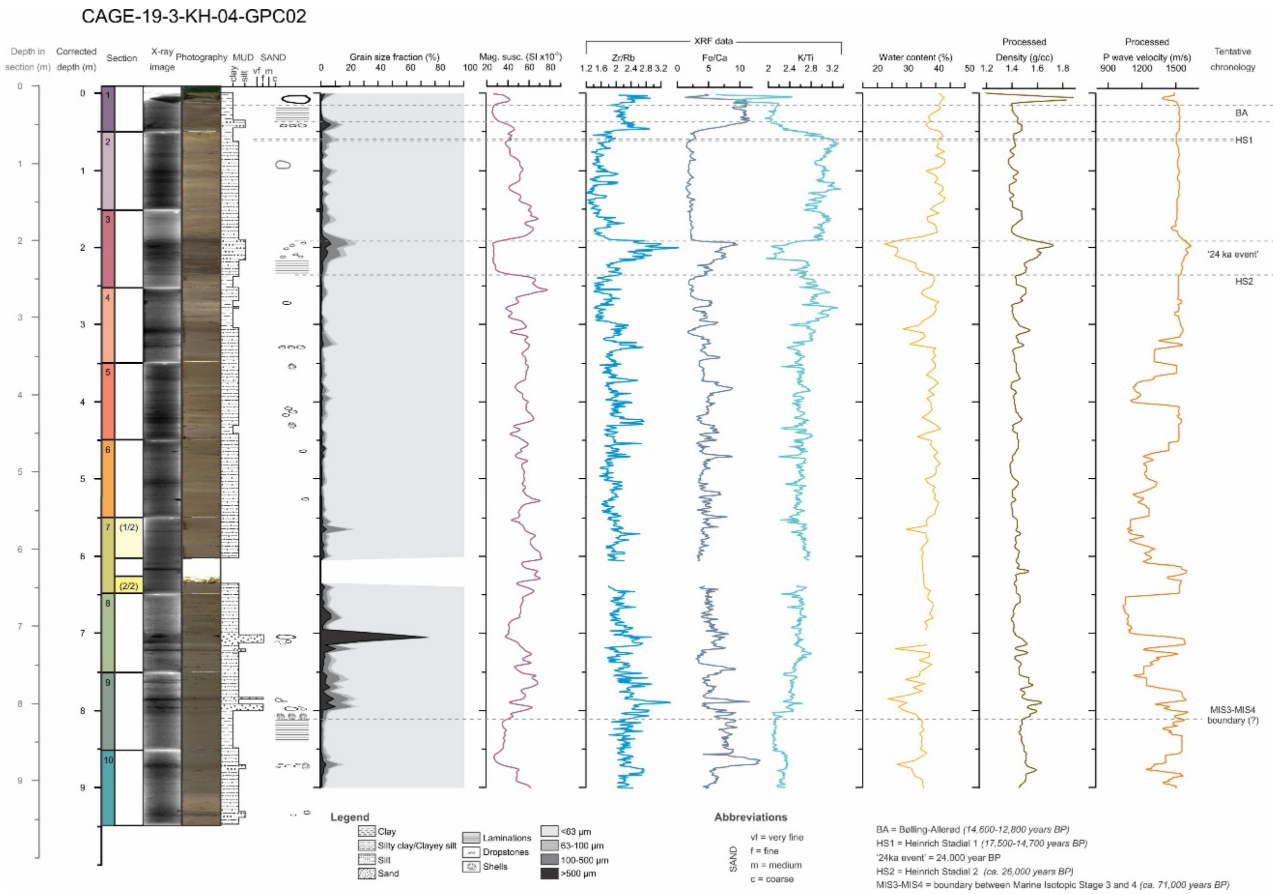

Figure S6. Additional sedimentological data from calypso core C-4. Bulk density, P-Wave velocity, XRF mineral ratio logs, water content, and the visual core description, are included in addition to grain size and magnetic susceptibility presented in figure 2 in the main text.

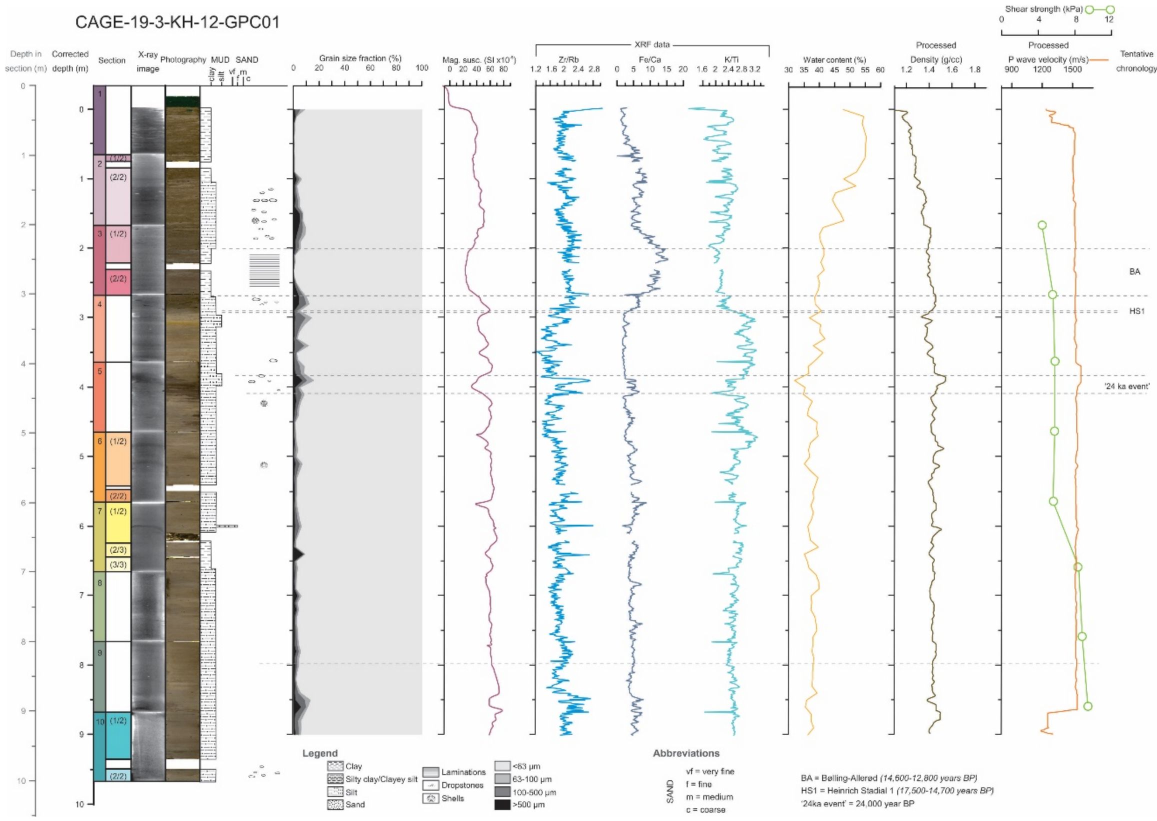

Figure S7. Additional sedimentological data from calypso core C-12. Bulk density, P-Wave velocity, XRF mineral ratio logs, water content, and the visual core description, are included in addition to grain size and magnetic susceptibility presented in figure 2 in the main text.

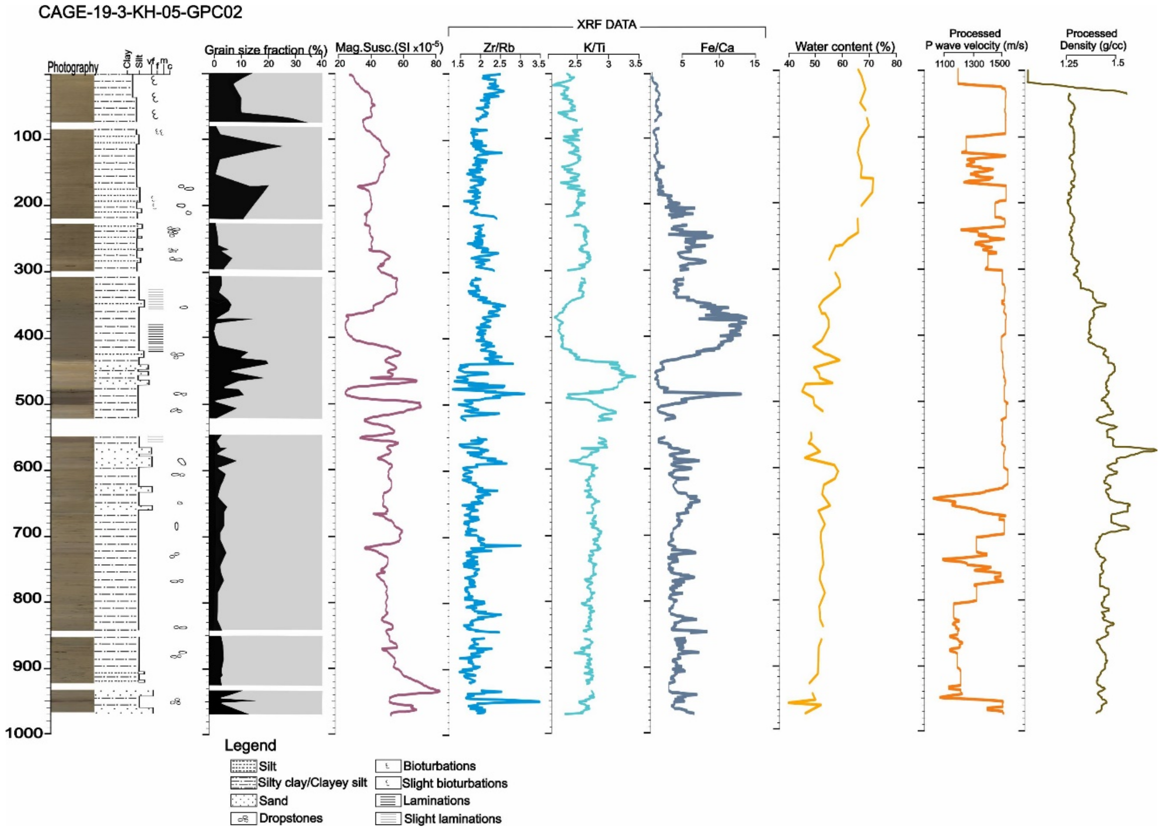

Figure S8. Additional sedimentological data from calypso core C-5. Bulk density, P-Wave velocity, XRF mineral ratio logs, water content, and the visual core description, are included in addition to grain size and magnetic susceptibility presented in figure 2 in the main text. The grain size analyses for the upper 2 m has a poor sampling rate of 20 cm and has a large uncertainty associated. The apparent increase in the percentage of sediment > 63 µm is not necessarily representative of the sediment distribution of the sequence Holocene period along this core.

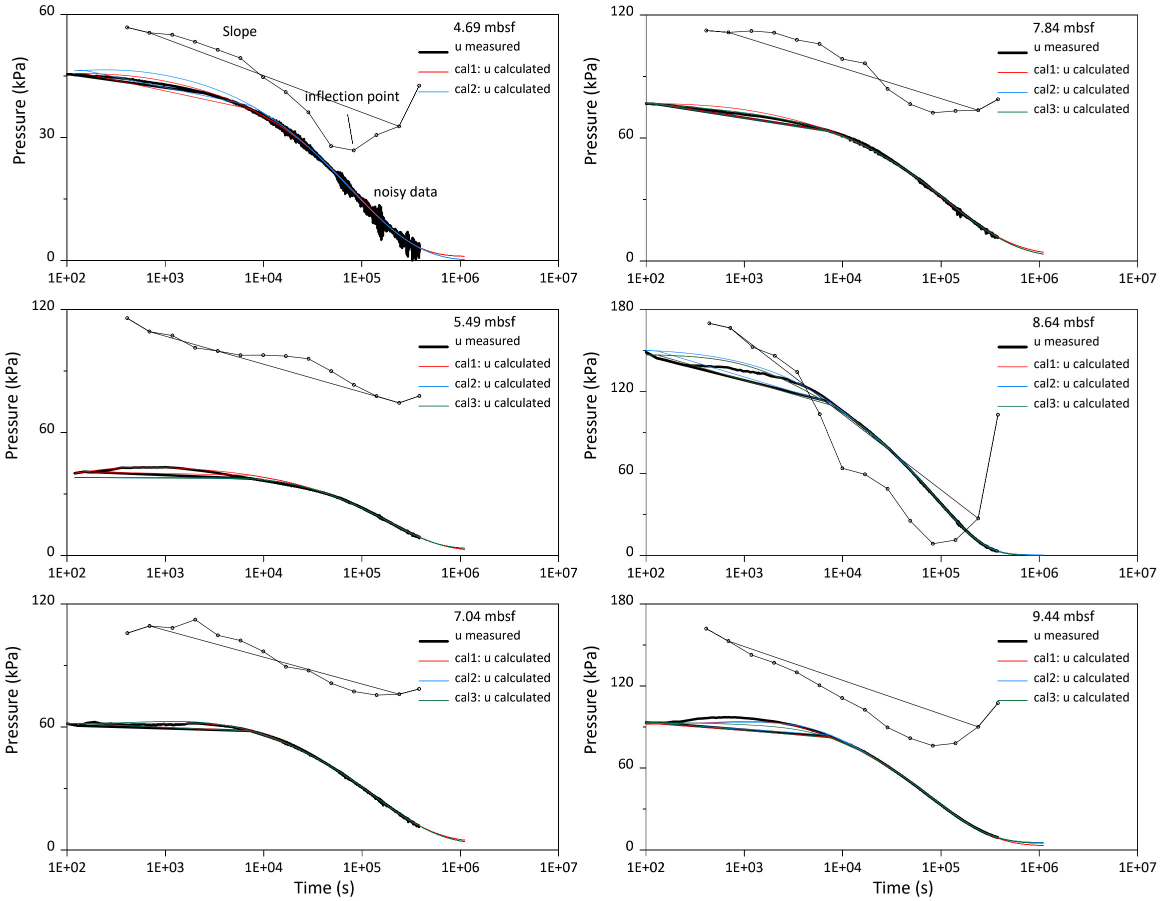

Figure S9. Pzm5. Three runs for the six deepest sensors with three different set of parameters giving similar pore-water dissipation curves. The full range of pore-water pressure dissipation data are also plotted (black line). $\frac{\partial \Delta u}{\partial(\ln(t))}$ values are added to the diagram showing for some sensors the inflection point which corresponds to the $\left(\frac{\partial^2 \Delta \boldsymbol{u}}{\partial \boldsymbol{ln}(\boldsymbol{t})^2} > \mathbf{0}\right)$ criteria.

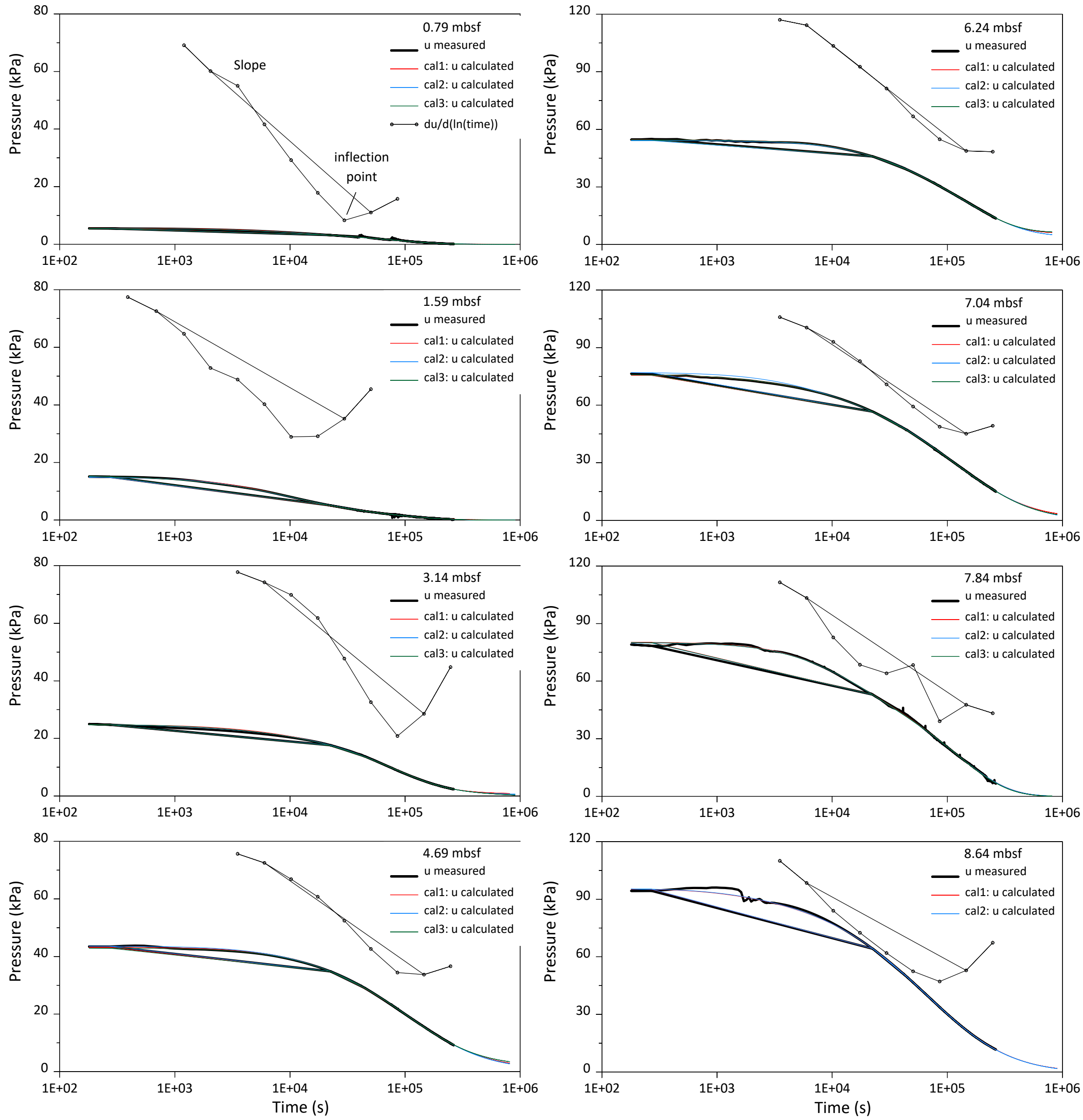

Figure S10. Pzm12W. Three runs for each sensor with three different set of parameters giving similar pore-water dissipation curves. The full range of pore-water pressure dissipation data are also plotted (black line). $\frac{\partial \Delta \mathrm{u}}{\partial(\ln(\mathrm{t}))}$ values are added to the diagram showing for some sensors the inflection point which corresponds to the $\left(\frac{\partial^2 \Delta \boldsymbol{u}}{\partial \boldsymbol{ln}(\boldsymbol{t})^2} > \mathbf{0}\right)$ criteria.

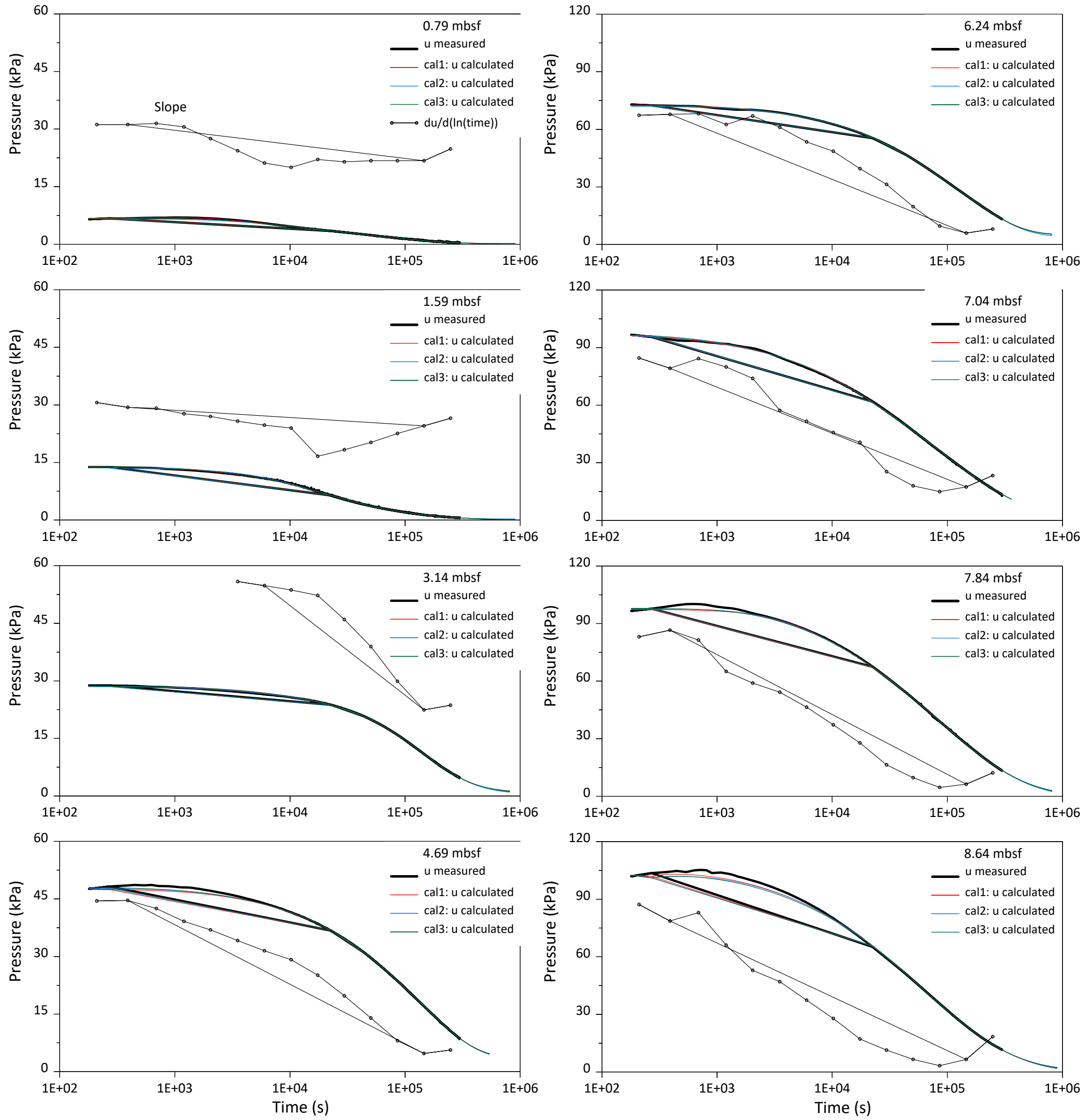

Figure S11. Pzm12E. Three runs for each sensor with three different set of parameters giving similar pore-water dissipation curves. The full range of pore-water pressure dissipation data are also plotted (black line). $\frac{\partial \Delta \mathrm{u}}{\partial(\ln(\mathrm{t}))}$ values are added to the diagram showing for some sensors the inflection point which corresponds to the $\left(\frac{\partial^2 \Delta \boldsymbol{u}}{\partial \boldsymbol{ln}(\boldsymbol{t})^2} > \mathbf{0}\right)$ criteria.

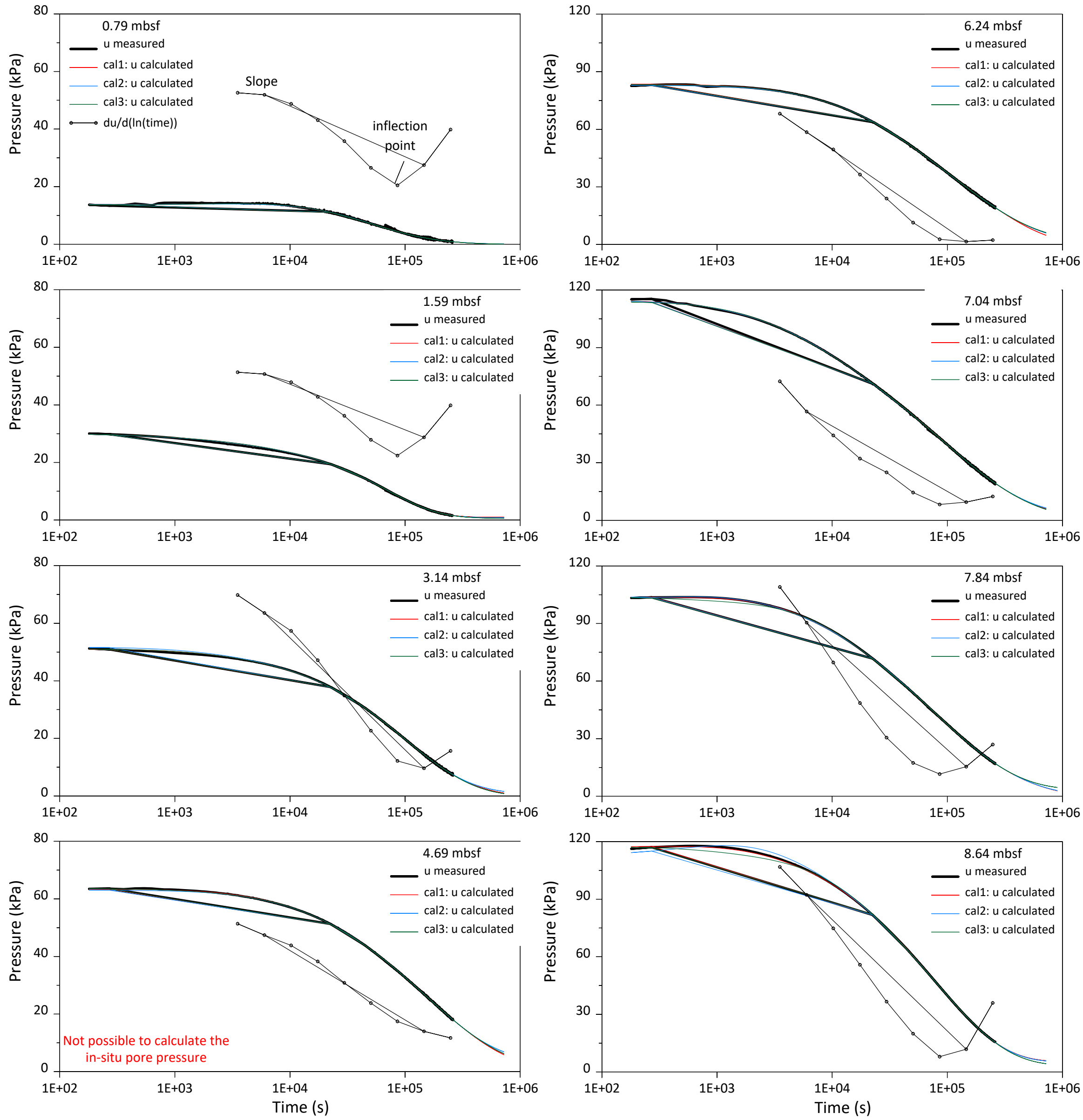

Figure S12. Pzm4W. Three runs for each sensor with three different set of parameters giving similar pore-water dissipation curves. The full range of pore-water pressure dissipation data are also plotted (black line). $\frac{\partial \Delta u}{\partial(\ln(t))}$ values are added to the diagram showing for some sensors the inflection point which corresponds to the $\left(\frac{\partial^2 \Delta u}{\partial ln(t)^2} > 0\right)$ criteria.

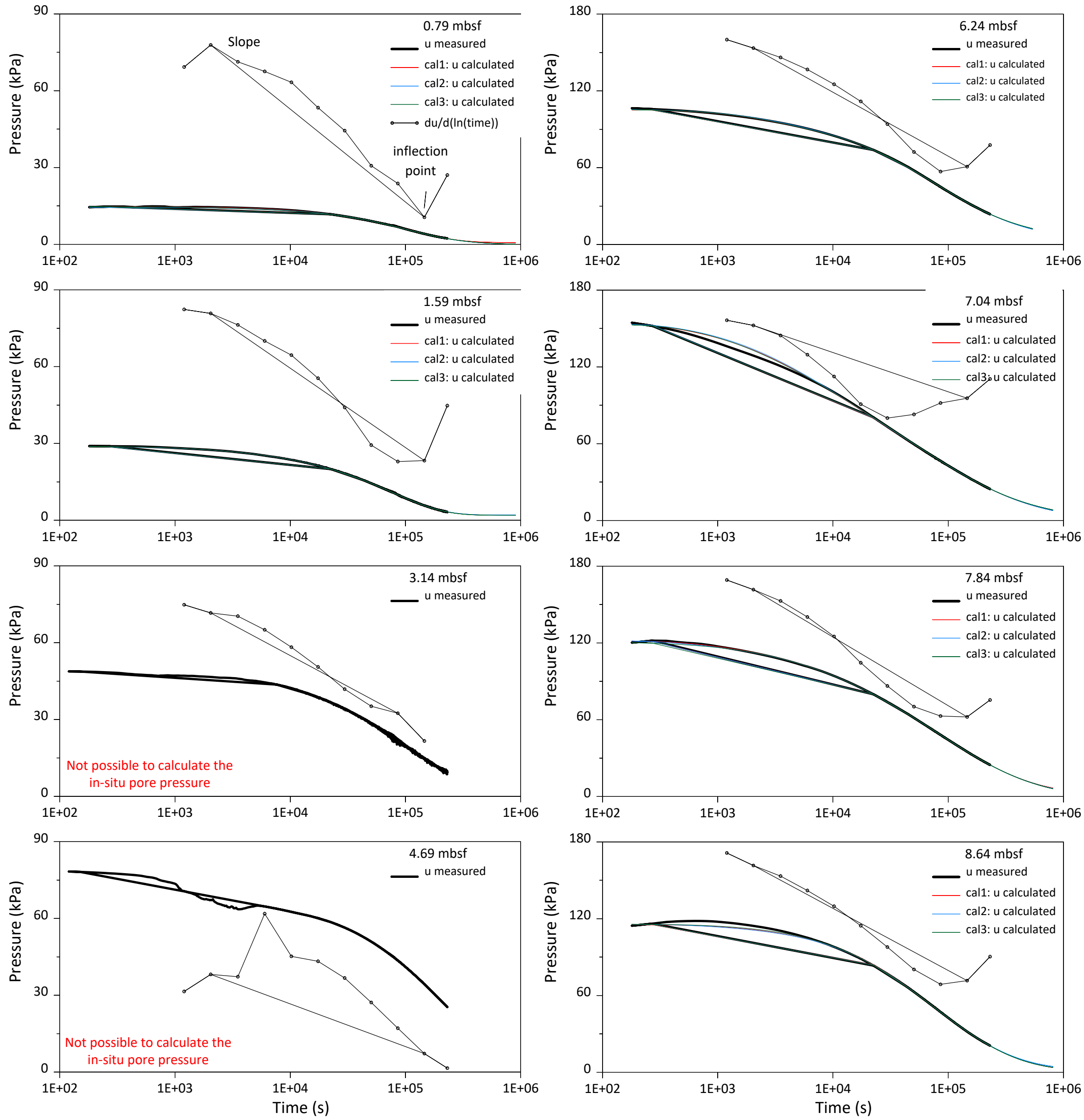

Figure S13. Pzm4E. Three runs for each sensor with three different set of parameters giving similar pore-water dissipation curves. The full range of pore-water pressure dissipation data are also plotted (black line). $\frac{\partial \Delta u}{\partial(\ln(t))}$ values are added to the diagram showing for some sensors the inflection point which corresponds to the $\left(\frac{\partial^2 \Delta u}{\partial ln(t)^2} > 0\right)$ criteria.

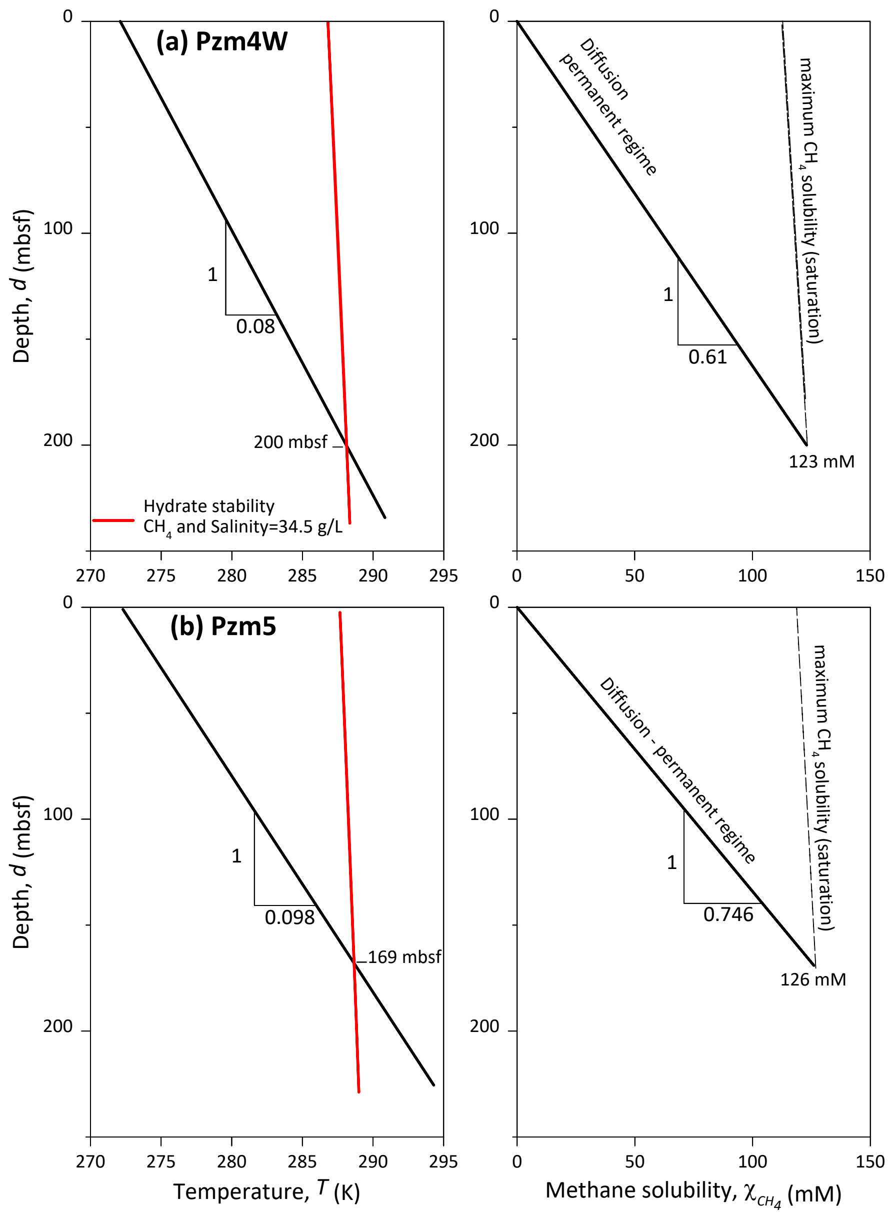

Figure S14. Methane solubility at sites (a) Pzm4E and (b) Pzm5.

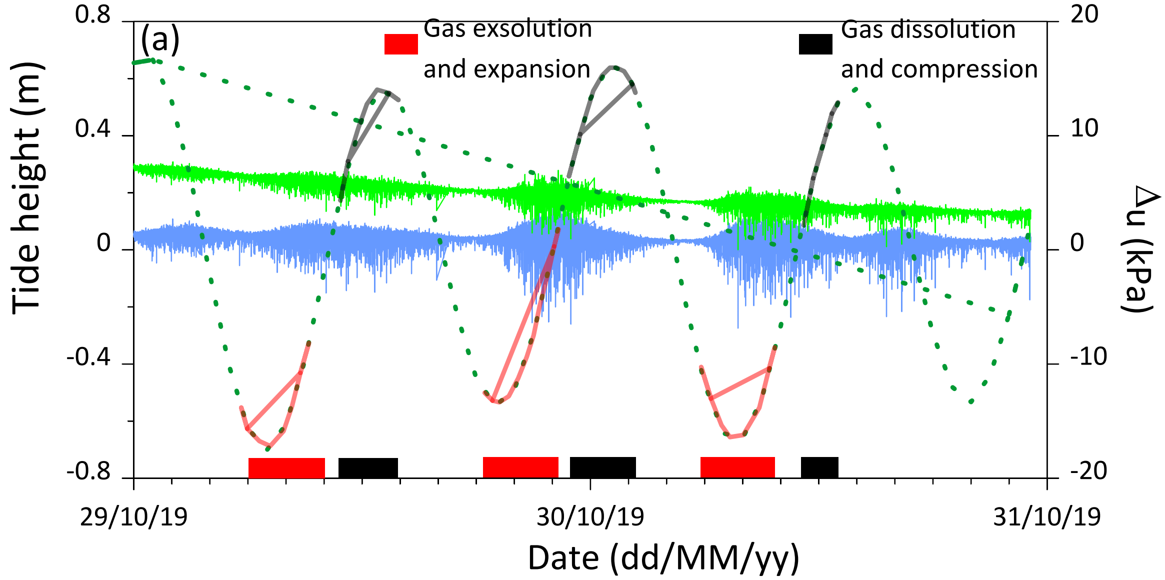

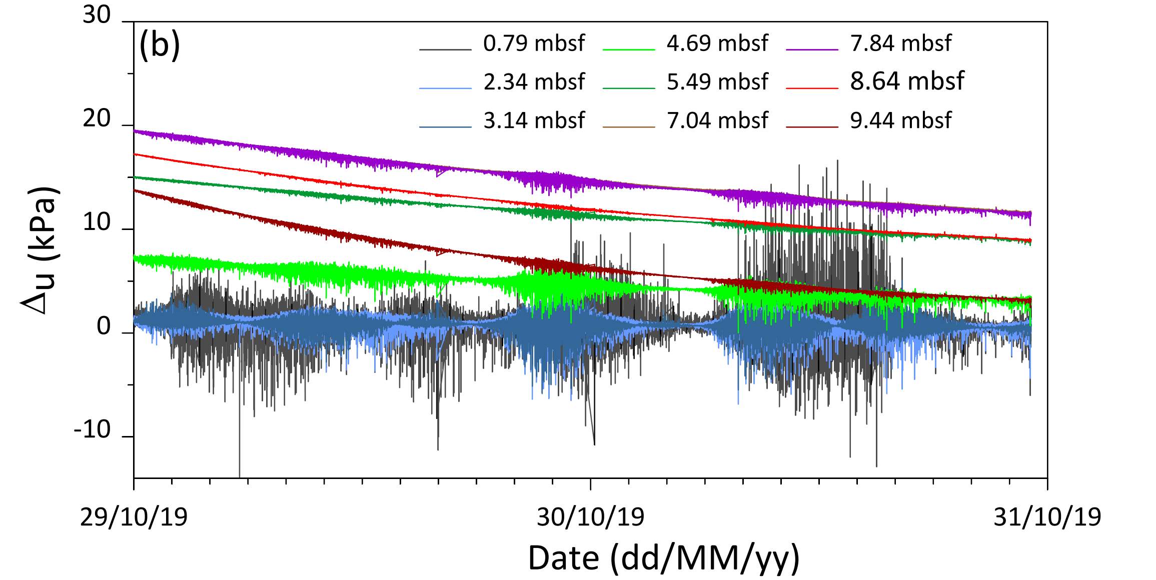

Figure S15. Site Pzm5 (a) Tidal height obtained at the piezometer location from the TPXO 9.0 global tidal model is shown as dashed line compared to Δu versus time at 3.14 and 4.69 mbsf. Red periods correspond to gas exsolution and expansion while black periods indicate gas dissolution and compression. (b) Δu versus time for the 9 sensors along Pzm5 showing Δu perturbations mainly during low and ascending tide cycles. The perturbation of Δu is proportional to the gas content [Garziglia et al., 2021].

Simplified name	Depth (m)	Station name	Quality
C-05	0.8	KH-05-PZM2	Very good
C-05	2.3	KH-05-PZM2	Very good
C-05	3.1	KH-05-PZM2	Good to Fair
C-05	5.49	KH-05-PZM2	Poor
C-05	8.6	KH-05-PZM2	Poor
C-05	9.4	KH-05-PZM2	Poor
C-12	0.84	KH-12-PZM3	-
C-12	2.3	KH-12-PZM3	Good to Fair
C-12	5.5	KH-12-PZM3	Poor

Table S1. Incremental loading oedometer tests carried out on sediment cores recovered from two investigated sites.

References

Abuel-Naga, H. M., and M. J. Pender (2012), Modified Terzaghi consolidation curves with effective stress-dependent coefficient of consolidation, *Géotechnique Letters, 2*(2), 43-48.

Astm, D. (2004), 2435, *Standard Test Methods for One Dimensional Consolidation Properties of Soils using Incremental Loading*.

ASTM International (2006), Standard test method for one-dimensional consolidation properties of saturated cohesive soils using controlled-strain loading (Standard D4186–06), in Annual Book of ASTM Standards, vol. 04.08, Soil and Rock (I), pp. 1–15, West Conshohocken, Pa

Burns, S. E., and P. W. Mayne (1998), Monotonic and dilatory pore-pressure decay during piezocone tests in clay, *Canadian Geotechnical Journal, 35*(6), 1063-1073.

Garziglia, S., N. Sultan, Y. Thomas, S. Ker, B. Marsset, X. Bompais, P. Woerther, C. Witt, A. Kopf, and R. Apprioual (2021), Assessing spatio-temporal variability of free gas in surficial cohesive sediments using tidal pressure fluctuations, *Journal of Geophysical Research: Earth Surface*, *126*(10), e2021JF006131.

Kim, Y., and S. R. Lee (2000), Prediction of long-term pore pressure dissipation behavior by short-term piezocone dissipation test, *Computers and Geotechnics*, *27*(4), 273-287.

Knies, J., and S. Vadakkepuliyambatta (2019), CAGE19-3 Cruise Report: Calypso giant piston coring in the Atlantic-Arctic gateway–Investigation of continental margin development and effect of tectonic stress on methane release, *CAGE–Centre for Arctic Gas Hydrate, Environment and Climate Report Series*, *7*.

Lunne, T., and M. Long (2006), Review of long seabed samplers and criteria for new sampler design, *Marine Geology*, *226*(1-2), 145-165.

Spivey, J. P., W. D. McCain, and R. North (2004), Estimating density, formation volume factor, compressibility, methane solubility, and viscosity for oilfield brines at temperatures from 0 to 275 C, pressures to 200 MPa, and salinities to 5.7 mole/kg, *Journal of Canadian Petroleum Technology*, *43*(07).

Sultan, N., and S. Lafuerza (2013), In situ equilibrium pore-water pressures derived from partial piezoprobe dissipation tests in marine sediments, *Canadian Geotechnical Journal*, *50*(12), 1294-1305.